SmokeBot

Mobile Robots with Novel Environmental Sensors for Inspection of Disaster Sites with Low Visibility

Grant agreement no: 645101

Project start: January 1, 2015

Duration: 3.5 years

Deliverable 1.1

Technical Description of Mechanical Pivoting Radar (MPR)

Due date: month 11 (November 2015)

Lead beneficiary: FHR

Dissemination Level: Public

Main Authors:

Simon Kueppers (FHR)
Reinhold Herschel (FHR)
Gunnar Briese (FHR)
Sandra Nowok (FHR)
Daniel Noethen (FHR)
Harun Cetinkaya (FHR)

Proofreading:

Stefan Lang (FHR)
Reinhold Herschel (FHR)

Version History:

1.0: Initial Version, sk, Nov. 27, 2015

Table of Contents

Table of Contents 3
1. Introduction 5
1.1. Motivation 5
1.2. Purpose of the Document 6
1.3. Structure of the Document 6
2. FMCW Radar Module 7
2.1. Working principle of a Radar System 7
2.2. FMCW based Radar Systems 8
2.3. Radar Module Architecture 11
2.4. Module Characterization 14
2.4.1. Output Power 14
2.4.2. IF Bandwidth 15
2.5. Antenna Considerations 15
2.5.1. RF based Geometric Imaging 16
2.5.2. Elliptical Dielectric Lens 18
2.5.3. Radiation Pattern 19
2.5.4. Feeding Element and Antenna Realization 21
3. 2D Mechanical Pivoting Radar 22
3.1. Concept and Design 22
3.2. Implementation 24
3.2.1. 80 GHz FMCW Radar Module 26
3.2.2. Slip Ring 27
3.2.3. Stepper Motor 28
3.2.4. Motor Controller Board 30
3.2.5. Radome 31
3.2.6. Fully Integrated MPR 32
3.3. Electrical Interface 34
3.4. MPR Specifications 36
3.5. Image Formation Algorithm 37
3.6. Experimental Evaluation of the 2D MPR 42
3.6.1. Comparison of different Antenna Aperture sizes 43
3.6.2. Comparison of different RF Sweep Bandwidths 46
3.7. Data Processing Algorithms 48

3.8. ROS Interface Description 50
3.8.1. Introduction 50
3.8.2. Node description 51
3.8.3. Parameters and Data Structures 52
4. 3D Mechanical Pivoting Radar 54
4.1. Mechanical and Electrical Setup 54
4.2. Image Formation Algorithm 61
4.3. Imaging Example 62
4.4. Preliminary MIMO Performance estimation 63
5. Summary 66
6. List of Figures 68
7. List of Tables 70
8. Appendix 71
8.1. MPR Quick Start Guide 71

1. Introduction

1.1. Motivation

In many emergency scenarios the availability of precise information about the conditions directly at the center of the disaster site is crucial for guiding rescue actions as well as potential counter-measures. Unfortunately the critical sites are often hard to reach as well as restricted in visibility by dangerous gases, smoke or dust. In these cases unmanned vehicles have proven to significantly lower the risk for the emergency team. Remotely driven robots can access places where the conditions do not allow sending people for investigation. Therefore vehicles have to be developed which can act under these conditions allowing a remote user to keep orientation in the unknown environment and obtain the information needed for planning and coordination of later measures. This ability will rely on a set of sensing systems. A key part of this sensor suite is a radar camera which can provide 3D information about the close environment with sufficient resolution to identify the structure of the site as well as critical objects. In contrast to a purely optical approach, a radar based device is only marginally restricted by fog or smoke so that especially in the case of fire it clearly outperforms ordinary camera or laser scanner systems.

The radar camera (Task 1.2 and 1.3) is based on a Multiple-Input-Multiple-Output[1] antenna concept which allows 3D real-time vision up to 50 meters in front of the vehicle. This device forms the hardware basis for software defined work packages in the project. The hardware development involves integrated circuit and PCB design, manufacturing and testing. Therefore, actual hardware will be available in a later stage of the project schedule. Obviously the development of the software tools for imaging and sensor fusion cannot wait until the radar camera is ready to be used. To allow parallelization of hardware and software development a preliminary radar imaging system was developed within the first stage of the project. This mechanically pivoted monostatic Radar provides 2D distance information 360° around the vehicle to provide first data to be fused with an additional laser scanner. This way sensor fusion and first remote control tests can be performed enabling progress of the project in all work packages. Additionally, the 3D scan capability of the MPR allows the generation of images in the antenna far-field that are equivalent to the MIMO sensor based images provided by the radar camera. Although not available in real-time these images will give an impression of the performance that is to be expected from radar camera module and can be used as basis for algorithm and hardware development.

[1] Also known as MIMO

1.2. Purpose of the Document

The aim of this deliverable is to present the results of the development of the MPR which was the focus of Task 1.1. The MPR design will be presented starting from the working principle of the used radar sensor, discussing the antenna design, the mechanical setup and the interface description. Imaging algorithms and concepts for image post-processing are introduced. System parameters such as antenna aperture size and radar bandwidth are discussed in terms of their impact on imaging quality. This includes the demonstration of 2D and 3D imaging results. The document therefore gives an impression of the first radar sensing module developed in the SmokeBot project from mechanical design to digital post-processing. Additionally at this early project stage, this document will serve as guideline for other project partners using the device as a tool for their contribution to the project.

1.3. Structure of the Document

The deliverable consists of 3 major parts. The first part describes the principle of the radar module starting from a review of its basic principle of operation. This is followed by the presentation of the modules system architecture including the definition of required interfaces. A brief description of the module's hardware integration and packaging concludes the module design part. It is complemented by a detailed discussion of the radar module's performance based on its experimental characterization. Beside the active part of the radar module the antenna is crucial for the performance of the imager. It is introduced theoretically and discussed based on simulated far field data. The second part of the document analyzes the design, implementation and performance of the 2D MPR which is part of the Description of Work. The mechanical setup is described as well as the electrical interfaces. To provide a guideline for potential users of the module technical specifications are listed. Additionally, a summary of these informations will be made available as a Quick Start Guide to enable our project partners an easy implementation of the developed system. Imaging algorithms are presented and digital post-processing algorithms are proposed for evaluating the acquired radar data. To ensure the compatibility of the MPR with other modules on the robotic platform the control algorithms have to be implemented in the standardized Robotic Operation System[2]. The interface based on a ROS node implementation will be presented for the 2D system. Finally, generated 2D plots are shown for different parameters of the radar, such as bandwidth or antenna size, to give information for the definition of suitable operation modes. The last part of the document describes the MPR based 3D imaging system. Differences in mechanical and electrical design are outlined in reference to the 2D version. Also for this setup images are shown. In contrast to the 2D images the 3D data can be used to generate image prediction for different MIMO technologies which supports the design of the MIMO array topology as well as later software based work packages within the project.

Therefore, this deliverable does not only provide an impression of the current status of the technological progress but should also serve as valuable tool for further steps towards a successful implementation of next generation mobile sensing systems.

[2] ROS (http://www.ros.org)

2. FMCW Radar Module

In order to illustrate the internal functioning of the MPR, first the basic operation principle of a FMCW[3] radar system is explained using the simple pulse based radar system as a starting point. In addition, the practical realization of the FMCW radar module used in the MPR is shown, alongside with its performance characteristics.

2.1. Working principle of a Radar System

The common principle of Radar[4] systems is to use the propagation and reflection characteristics of electromagnetic waves in order to detect targets or acquire their distance, speed or movement direction. In the context of this work, the focus shall be set on primary radar systems, which in contrast to secondary radar systems do not require actively transmitting targets, but instead rely on the reflection properties of the target's surface to reflect the electromagnetic wave back to the receiver. Fig. 2.1 illustrates the detection and ranging of a single target, using a pulsed radar system, where a high frequency transmitter is being used to transmit a short pulse of electromagnetic energy into a medium with a specific propagation velocity. When a target is being hit by this high-frequency pulse, a small portion of the transmitted energy is reflected in form of electromagnetic waves which can be detected by an adequately sensitive detector, connected to the receive antenna.

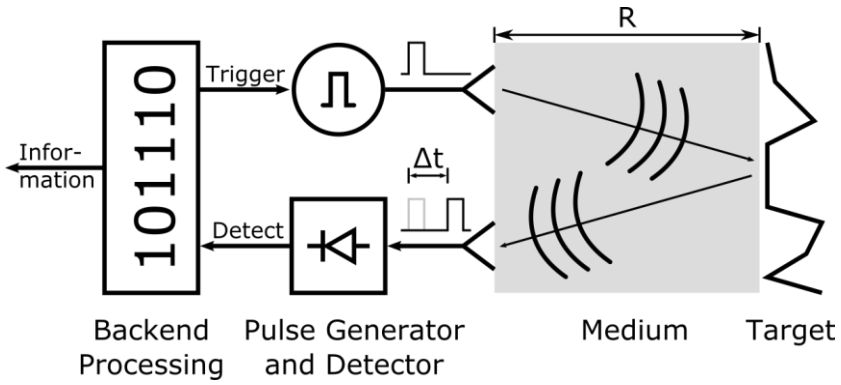

Fig. 2.1: Detection and Ranging using a pulsed radar system

Taking into account the propagation velocity **c** of electromagnetic waves in the used medium, it can be shown that the basic relationship between the distance **R** from the radar system to an immobile target and the time delay **Δt** from the transmission to reception of the electromagnetic pulse can be expressed as shown in Eq. 2.1.

$$R = \frac{c}{2}\Delta t \qquad \textbf{Eq. 2.1}$$

In other words, the distance to the target is proportional to half the round trip time the electromagnetic wave requires to travel from the transmitter to the target and back to the receiver. Since the energy of the reflected electromagnetic wave is dependent on the target's surface, a sensitive radar receiver needs a high dynamic range in order to pick up the faint reflections from targets having low radar-cross-

[3] Frequency Modulated Continuous Wave
[4] RADAR: Radio Detection and Ranging

section[5]. While the pulsed radar system easily demonstrates the basic working principle of radar systems, there are more sophisticated types of radar systems available as will be shown in the following chapter.

2.2. FMCW based Radar Systems

By modifying the short pulse of single-tone frequency from Section 2.1 to a linear frequency ramp as shown in Fig. 2.3, a Frequency Modulated Continuous Wave Radar System can be realized (cp. Fig. 2.2).

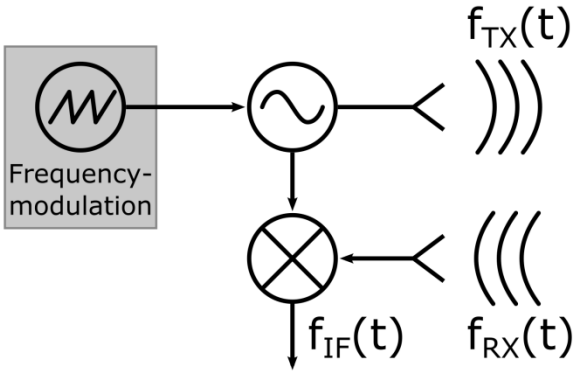

Fig. 2.2: FMCW Radar System Architecture

It can be shown that such a system has some advantages compared to a pulsed radar system shown in Fig. 2.1. One advantage of such a linear FMCW radar system is the fact that the detection and ranging of such a system is available in a continuous fashion, because the transmission and reception of the electromagnetic waves occur simultaneously. Furthermore, to achieve a good spatial resolution, pulsed radar systems require the use of extremely short pulse lengths, which gets increasingly harder to realize, when a high spatial resolution is required. In contrast to that, the range resolution in linear FMCW based radar system is merely a function of the sweep bandwidth $\mathbf{BW_{RF}}$.

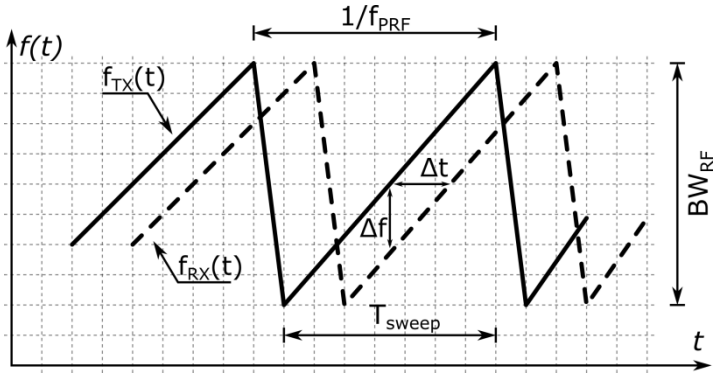

Fig. 2.3: FMCW Radar System working principle

The basic working principle of a FMCW radar system, as shown in Fig. 2.3 is very similar to that of the pulsed radar (Fig. 2.1), where a propagation delay $\mathbf{\Delta t}$ of an electromagnetic wave through a medium is used to determine the distance to a target.

[5] Often referred to as RCS

The figure illustrates a transmitted signal (solid line) showing the momentary transmit frequency $\mathbf{f_{TX}(t)}$ that changes linearly over time. Indicated by the dashed line is the delayed signal reflected from a single target as seen by the receive antenna. Due to the use of a linear modulation, the received signal has a specific frequency offset **Δf** with respect to the momentary transmit signal, at each point in time during a frequency sweep. Thus, if this frequency difference can be extracted from the high frequency RF signals by means of a frequency mixer shown in Fig. 2.2, the range to the target can be determined by measuring the resulting frequency difference. This frequency offset, once converted to the intermediate frequency $\mathbf{f_{IF}}$ (typically in the range up to several MHz) can then be further processed by operational amplifers, filters and analog to digital coverters and evaluated digitally.

From Fig. 2.3 the basic relationship between **Δf** and **Δt** (and thus the distance **R** from Eq. 2.1), expressed as a linear function can be derived (see Eq. 2.2).

$$\Delta f = \frac{BW_{RF}}{T_{sweep}} \Delta t \qquad \textbf{Eq. 2.2}$$

Using Eq. 2.1 to calculate the target distance **R** in conjunction with the definition of the offset-frequency **Δf** from Eq. 2.2 yields Eq. 2.3.

$$R = \frac{c}{2} \frac{T_{sweep}}{BW_{RF}} \Delta f \qquad \textbf{Eq. 2.3}$$

Eq. 2.3 shows, that the distance **R** and offset frequency **Δf** correspond linearly by a factor of $c * T_{sweep} \big/ 2 * BW_{RF}$, with **c** being the propagation velocity of the electromagnetic wave and $\mathbf{T_{sweep}}$ being the duration of the linear modulated frequency sweep that covers a frequency bandwidth of $\mathbf{BW_{RF}}$.

From Fig. 2.3 it can also be seen, that the pulse repetition frequency[6] $\mathbf{f_{PRF}}$ can be almost as fast as the reciprocal sweep time $1/T_{sweep}$, only limited by the time required for the ramp to reset to its starting point. Therefore the measurement rate is often higher than those of pulsed radar systems.

It should be noted that for the sake of simplicity, all considerations up to this point assumed a single target reflection. However, it can be shown that all equations hold true for multiple targets, since the resulting signal can be expressed as a linear superposition of the reflected signals from all targets within the line of sight of the radar system. Furthermore only stationary targets and single slope frequency ramps have been discussed in this section, since further modes of operation are not relevant to the mechanically pivoted radar.

[6] Often referred to as PRF

In order to separate all the targets in the acquisition range of the radar and determine their particular distance, a fourier transform of the digitized intermediate frequency time domain signal is commonly employed. The resulting frequency domain representation is equivalent to the spatial domain, due to the linear relationship in Eq. 2.3. Also to reduce the leakage effect resulting from applying the periodic fourier transform to non-periodic signals, a window function such as hann or hamming for example can be applied prior to the fourier transformation. Fig. 2.4 shows an exemplary acquired radar time domain signal and its frequency domain representation, revealing a single strong target reflection at a distance of 0.6 meters (approx. 100 kHz) using an RF sweep bandwidth of 24 GHz and a sweep time of 10 milliseconds. In addition, several targets with multiples of 0.6 meters can be observed and are a result of multiple reflections that occur between the target and the radar module in the used experimental setup.

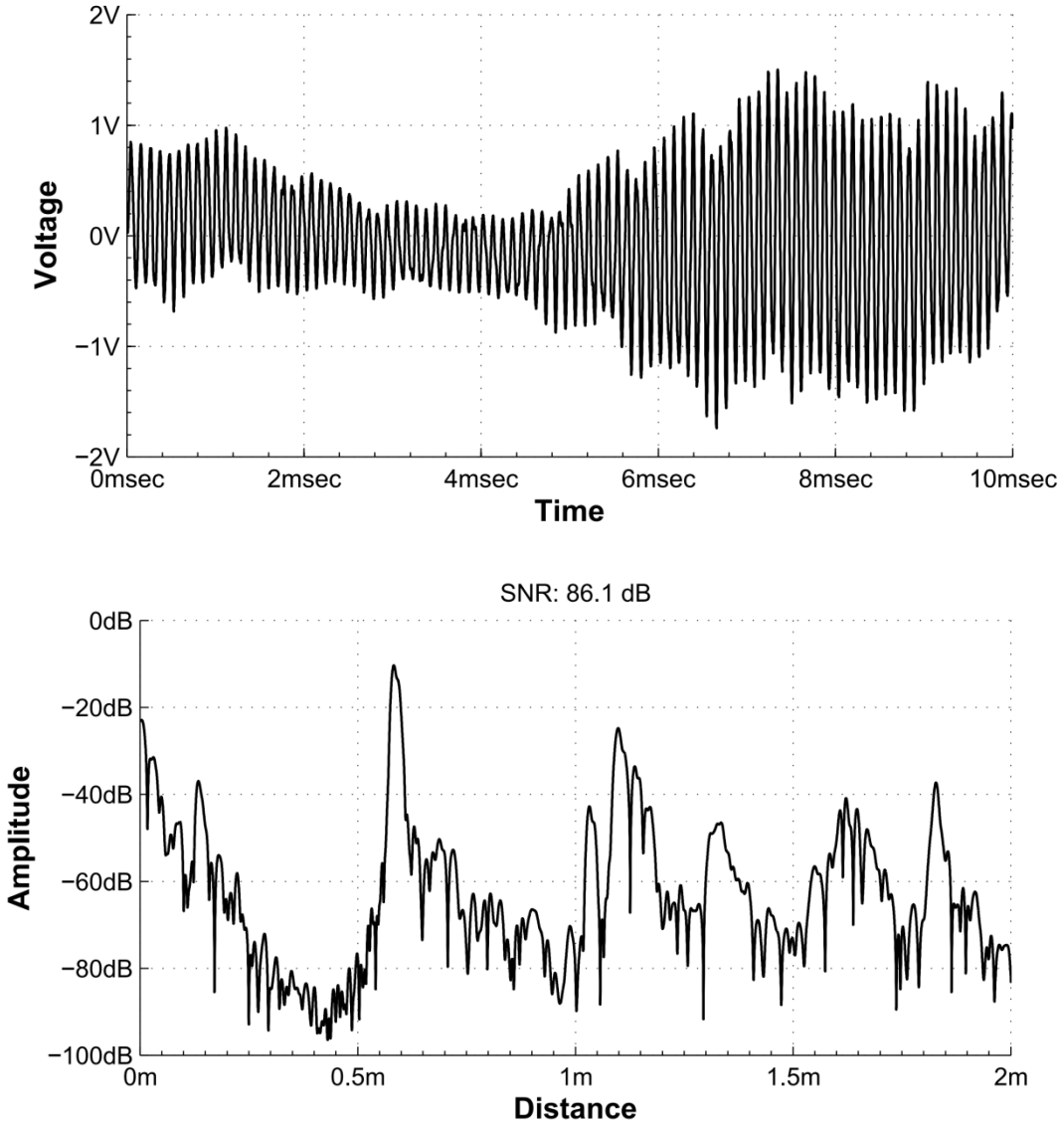

Fig. 2.4: Time domain and corresponding frequency/spatial domain representation

2.3. Radar Module Architecture

The mechanically pivoted radar, realized in Task 1.1 is based on an 80 GHz FMCW radar module (see Fig. 2.5) that has been developed at the Ruhr University in Bochum in conjunction with the Fraunhofer FHR[7]. In this section, a brief introduction about the radar module's architecture is given.

Fig. 2.5: Photograph of Radar Module in Case

The module's system realization is shown in Fig. 2.6. From the photograph, the separation between the high-frequency frontend (bottom) and an acquisition backend (top) is clearly visible. This not only allows for interchangeability of different frontend types with different acquisition backends, but also for a space efficient radar system assembly. Due to the fact that only the frontend board requires a special high-frequency circuit board substrate, also a very cost-effective system has been realized.

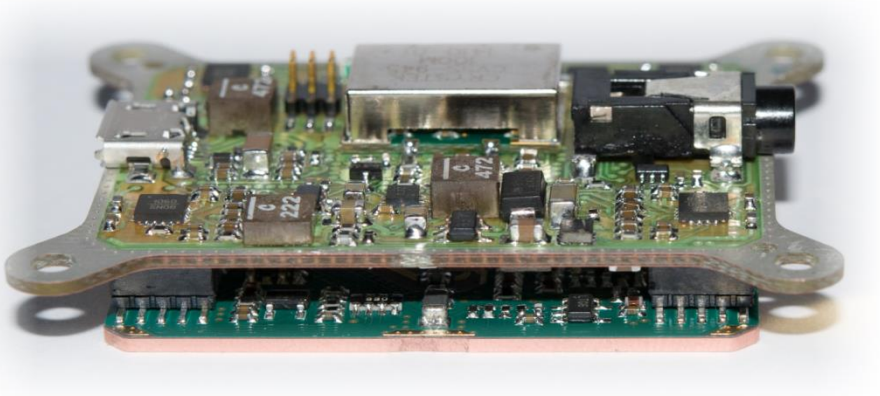

Fig. 2.6: Photograph of frontend and backend of the radar module

[7] Pohl, N.; Jaeschke, T.; Aufinger, K., "An Ultra-Wideband 80 GHz FMCW Radar System Using a SiGe Bipolar Transceiver Chip Stabilized by a Fractional-N PLL Synthesizer," in *Microwave Theory and Techniques, IEEE Transactions on*, vol.60, no.3, pp.757-765, March 2012(doi: 10.1109/TMTT.2011.2180398)

A more detailed view of the module's architecture is shown in Fig. 2.7. Starting from the high frequency frontend on the left, a fully custom monolithic microwave integrated circuit[8] developed at the Ruhr University Bochum is used for handling all high frequency signals. Its main purpose is the generation of a frequency tunable radio frequency signal in the range of 68 to 92 GHz that is being transmitted using a WR-10 flange embedded into the frontend substrate shown in the top left. Furthermore the MMIC holds the receive mixing downconverter in order to generate the intermediate frequency signal denoted as **IF+/-**, that contains all range-profile informations of the radar system. In order to generate the high linearity ramps necessary to employ the FMCW radar principle shown in section 2.2, two off-the-shelf phase locked loop chipsets are used. The frequency stabilization technique in this system has been realized by the use of an offset-PLL arrangement, which involves a fixed frequency as well as a frequency-sweeping phase locked loop. This stabilization concept allows the generation of highly linear sweep signals, by using a delta sigma modulator, while a high maximum sweep bandwidth of 24 GHz can be maintained at low phase noise levels.

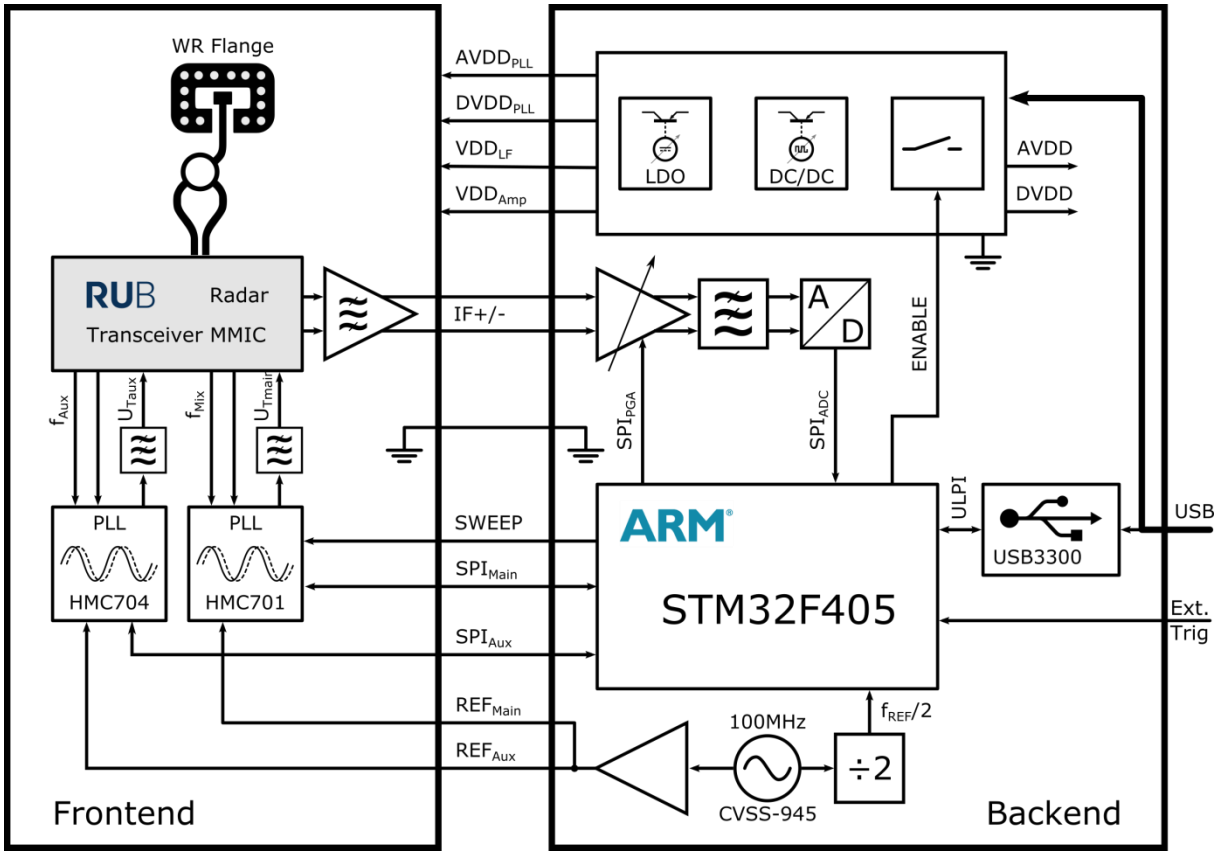

Fig. 2.7: Radar Module Architecture

Additionally an IF pre-amplifier with band-pass characteristic has been used in order to amplify the weak IF signals prior to the processing on the backend board, thus avoiding degradation of the signal-to-noise ratio caused by digital noise present on the backend circuit board. In order to utilize as much dynamic range as possible in the

[8] Pohl, N.; Klein, T.; Aufinger, K.; Rein, H.-M., "A Low-Power Wideband Transmitter Front-End Chip for 80 GHz FMCW Radar Systems With Integrated 23 GHz Downconverter VCO," in *Solid-State Circuits, IEEE Journal of* , vol.47, no.9, pp.1974-1980, Sept. 2012 (doi: 10.1109/JSSC.2012.2201272)

following signal processing stages, the band-pass characteristic of this amplifier is modelled, such that it approximately compensates the free-space path loss, by attenuating signals in the low frequency domain. Thus near targets, located at low IF frequencies, that typically produce strong reflections and high IF amplitudes will be equalized to the amplitude of targets that are further away and will thus show up at higher intermediate frequencies.

In the right half of Fig. 2.7, the backend portion of the radar module is shown. Following the IF signal processing chain, a programmable gain amplifier has been used to further amplify the IF signal in order to fully utilize the available dynamic range of the analog to digital converter. Note that the gain of this amplifier can be controlled by software, thus it can be adjusted to assure a signal level that is well matched to the backend digitization. Prior to the digitization, a high-order low-pass filter has been used to limit any aliasing artifacts from target reflections above the IF frequency range of about 400 kHz. Also, the filter incorporates a sufficiently strong ADC driver in order to deliver the necessary signal fidelity for the successive 16 Bit analog-to-digital converter with a sample-rate of 1MSa/s.

After digitizing the radar intermediate frequency signal, the sampled time-domain signal is being stored by employing a double-buffer arrangement in the STM32 microcontroller and is streamed out over a USB 2.0 interface to the connected computer. With this system, a high measurement repetition rate can be achieved, by allowing a simultaneous ADC acquisition, during the transmission of data acquired in the previous sweep. Therefore an almost continuous stream of USB data transmission can be realized.

Furthermore the microcontroller used in the backend of the radar module is able to control the power delivery to the radar frontend and may shut it down when idling, thus conserving power when operated from a battery. Regarding the power supply of the frontend, high effort has been put into to splitting and filtering of the different voltage rails, therefore achieving a better noise floor in the high-frequency RF signals as well as the in the IF frequency band.

2.4. Module Characterization

The radar module was characterized in its basic performance parameters which influence the quality of the images generated in a later stage. While the SNR is mainly dependent on the transmitted RF power, the resolution is given by the radar bandwidth. The used radar module is hermetically packaged so that only the RF transceiver port and the digitized intermediate frequency signal were accessible for experimental investigation. Therefore, the following will show the experimental characterization of the transmitted RF power and the frequency response of the IF port measured from the digitized data stream.

2.4.1. Output Power

The transmitted RF power was measured directly at the hollow metal WR10 port without the antenna. A stepped CW measurement was performed using an RF power meter and a 1 GHz step width. The radar module is specified to be capable of chirp bandwidths up to 25 GHz at a centre frequency of 80 GHz. Therefore, an RF frequency window ranging from 68 GHz to 95 Ghz was chosen to cover the full range of operation.

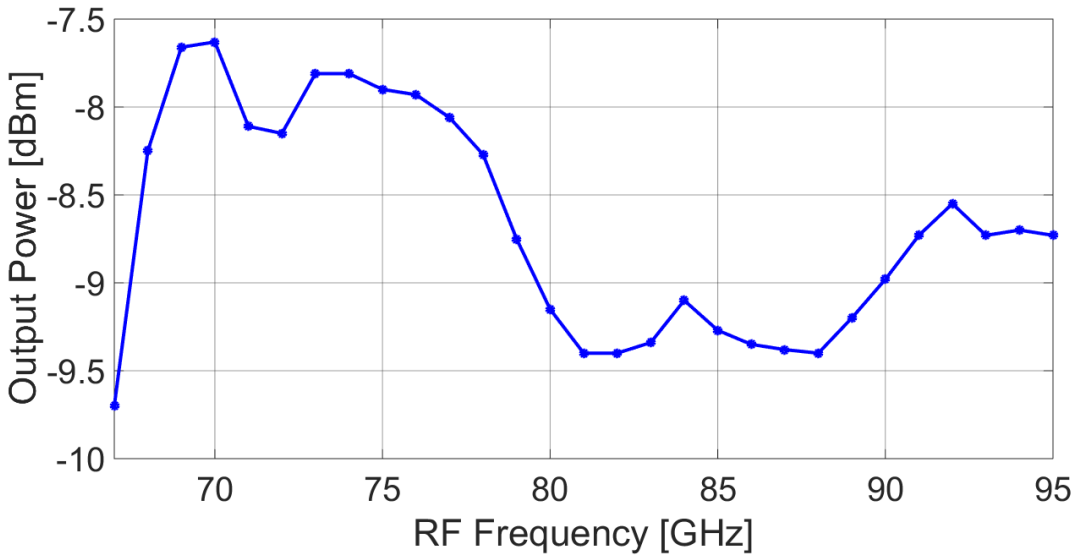

Fig. 2.8: Measured available transmit power of radar module

Fig. 2.8 shows the RF power transmitted by the radar module at the antenna flange as a function of frequency. At the centre frequency of 80 GHz the module transmits -9.2 dBm RF power. This increases towards the lower edge of band where a maximum power level of -7.6 dBm is reached. For lower frequencies the increasing loss of the WR10 waveguides such close to its cut-off frequency limits the transmission band. At the upper end of the band the transmitter power seems not to degrade so that the module is not restricted at this point by the transmitter side. The overall power fluctuation is limited to less than 2dB over the entire band of operation. No high frequency ripples are recognizable which could lead to rapid power fluctuations during the frequency chirp. Nevertheless a suitable calibration might be required to prevent the remaining target broadening due to frequency response caused modulation effects during the chirp duration.

2.4.2. IF Bandwidth

In succession to characterizing the transmitter side of the module, the IF path was investigated experimentally. Here the main focus was set on the frequency response of the IF side. A reference target moved in range towards and away from the radar was used while the chirp was active to generate an entire spectrum of IF signals. The free space path loss (FSPL) was compensated digitally after the measurement.

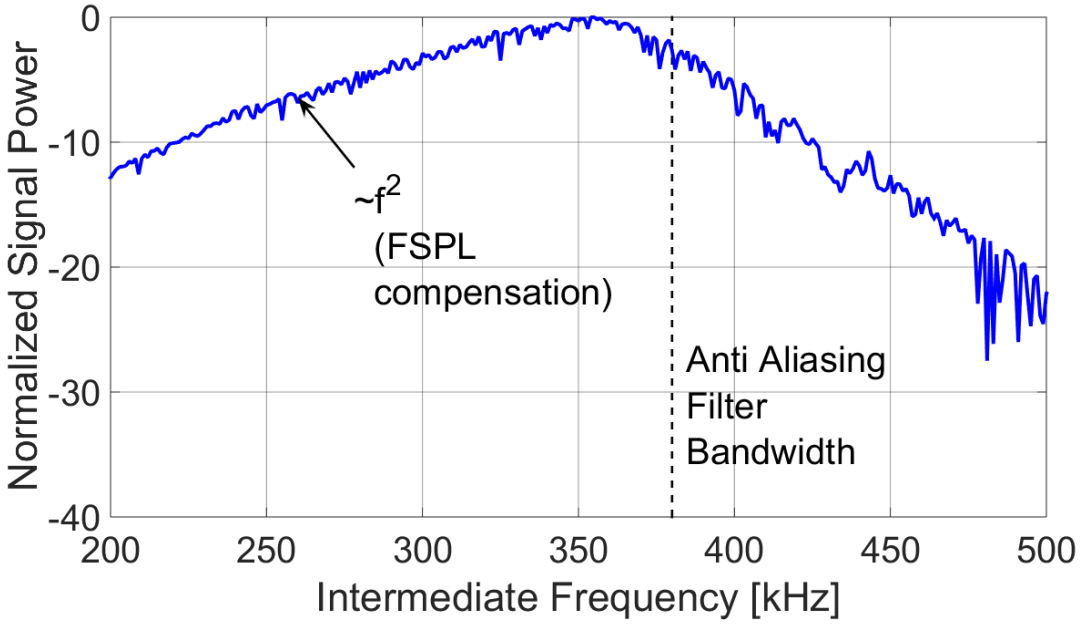

Fig. 2.9: IF Frequency response of the radar module

Fig. 2.9 shows the normalized signal strength of the generated IF signal as a function of frequency. The total IF characteristic of the module forms a bandpass filter. Within the range of operation below 350 kHz a quadratic high pass filter compensates for the FSPL[9] loss to maintain the full dynamic range over a wide range of distances. Additionally direct crosstalk within the module is effectively suppressed by this high pass filter. The sensitivity of the radar reaches its maximum at 360 kHz frequency offset before the upper band restriction inverts the slope to a low pass filter characteristic. This low pass filter has a 3dB bandwidth of 380 kHz. Due to the 1 MSa/s of the module's analogue to digital converter this bandwidth is well matched to the resulting Nyquist frequency of 500 kHz to prevent aliasing effects.

2.5. Antenna Considerations

Due to the modular nature of the WR-10 antenna interface on the radar module, a wide variety of antenna variants could potentially be used for the MPR application. This chapter presents two different antenna designs that have been selected for the use in the mechanical pivoting radar.

Due to the laser-scanning like operation principle of the mechanical pivoting radar, a small antenna beam width is required in order to achieve a high angular resolution. Having in mind the inverse relationship of beam width to antenna aperture size and the limited space availability for the mechanically pivoting radar, a compromise

[9] Free-space path loss

in spatial efficiency and angular resolution has to be made. A comparison of off-the-shelf WR-10 horn antenna shows that allowing for a maximum antenna length of about 50 mm, a beam width of about 10 degrees can be realized. In order to achieve a better angular resolution, dielectric lens antenna concepts have been considered for this application.

2.5.1. RF based Geometric Imaging

Radar based imaging is based on the measurement of the distance of reflecting objects for a whole set of azimuth and elevation angles. Ideally a radar beam with an infinitely small beamwidth would be used. In this case each radar measurement would only give the reflection at one discrete angle, which would enable the generation of images of unlimited resolution in azimuth and elevation. Unfortunately an infinitely small beamwidth is not physically possible. Therefore, the resolution of the image is limited by the opening angle of the antenna beam. The image can be seen as a convolution of the ideal radar image with the beam spot generated by the antenna.

For both, 2D and 3D radar measurement-systems developed in WP1.1, a small beamwidth is a crucial factor for high resolution imaging. The antenna forms the transition between the guided RF signals in the analogue front-end and the radiated field which is the basis of the remote radar imaging. Of course the efficient coupling of guided to radiated fields is a key to a distance measurement with high dynamic range. For imaging the direction of arrival is the second parameter which contains crucial information. Directing the radiation is the second important task fulfilled by the antenna. As stated in standard literature[10] any antenna can be understood as the summation infinitesimally small Hertzian dipoles, thus in consequence each part of the antenna surface forms a point source. The overall radiation characteristic is formed by the coherent summation of all small subradiators.

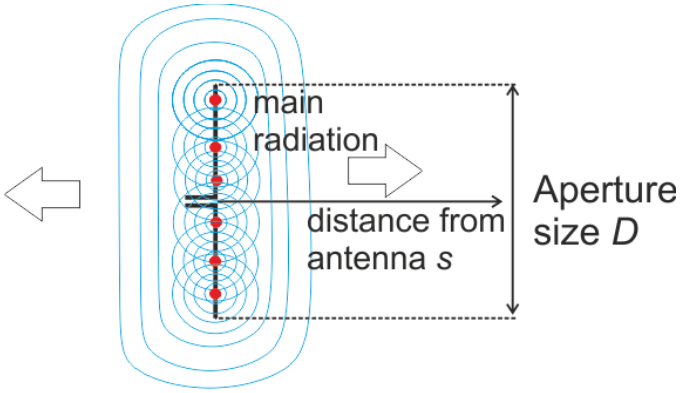

Fig. 2.10: Antenna as sum of omnidirectionally radiating elements

As shown in Fig. 2.10, the electromagnetic fields formed by each infinitesimally small part of the antenna form a common radiation field after some distance *s* from the radiator. With growing distance s the field can be approximated as plane wave, called the far field of the antenna. The minimum distance required for a valid plane wave approximation depends on the aperture size and is given by $s \gg \frac{2D^2}{\lambda}$.

[10] "Antenna Theory – Analysis and Design" (Second Edition) by C. A. Balanis

Since for valid far-field conditions the distance from the antenna has to be far larger than its aperture D the radiator can be seen as a point source. The coherent summation of all elementary waves is direction dependent. It is given by the Fourier transform of the current distribution on the aperture. Consequently a large aperture will lead to a small beamwidth and vice-versa.

If an antenna can be understood as the summation of infinitesimally small elements whose fields depend on the current density on the antenna surface a desired current distribution can also be obtained by an array of individual elements. In this case the current distribution is not continuous but discrete. The far-field is therefore given by a discrete Fourier transform. To avoid aliasing the angular domain, or in other words sidelobes, it must be ensured that the maximum phase shift between the array elements does not exceed +/-180°. This results in a maximum separation of λ/2. Using individual elements enables to adjust the relation of the discrete current distribution over the radiating array. This is commonly used for digital beam steering.

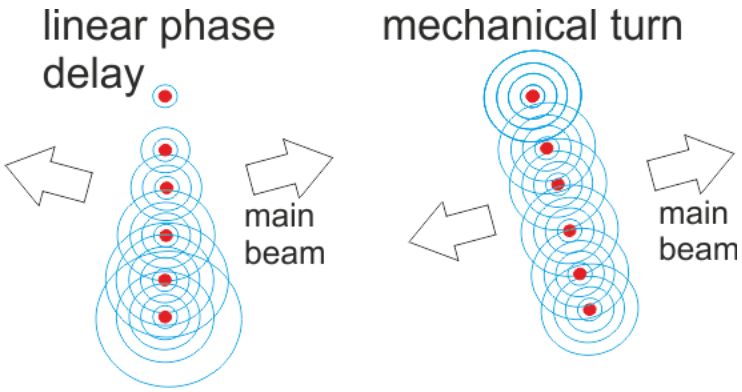

Fig. 2.11: Comparison of mechanical and phased array beam steering

Fig. 2.11 visualizes the equivalence of mechanical and electronical beam steering. In principle mechanically turning the antenna only changes the angle where all subradiators add up constructively. This can be artificially obtained by introducing a linearly increasing time delay over the array. For small angles the only difference is the inverse sign of the angular change of forward and back-travelling wave. In consequence, an entire angular range can be scanned either by a mechanically or an electronically steered antenna. While the electronical beam steering is employed in the MIMO based radar-camera in Task 1.1 and 1.2, the MPR uses mechanical beam steering. However, the obtained images are expected to be comparable for equal aperture sizes. It always has to be kept in mind that this holds true for far-field conditions. Depending on the distance of the detected objects from the imaging system near-field effects might lead to differences which have to be discussed while interpreting the specific results.

2.5.2. Elliptical Dielectric Lens

The evaluated lens antenna[11] uses a massive droplet-like PTFE body, fed by a metallic structure with a WR-10 waveguide flange as shown in Fig. 2.13.

The basic shape of the antenna follows a geometrical lens approach, where all quasi-optical rays of a single radiator at the feed-point should have the same delay time until they reach the targeted plane phase front shown in Fig. 2.12.

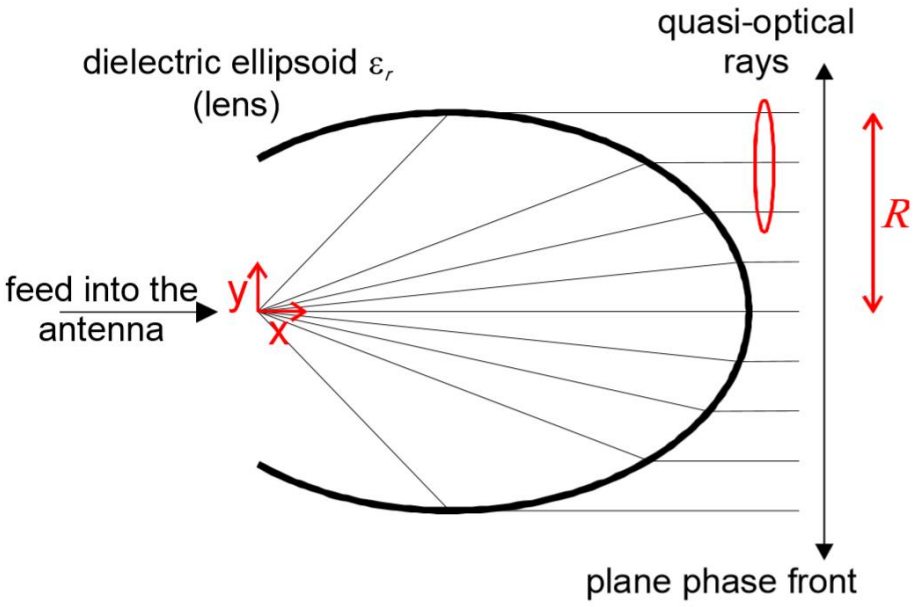

Fig. 2.12: Geometrical Design of Elliptical Lens

The geometrical-optical lens approach is a good choice in order to realize a directional antenna. All of the quasi-optical rays radiating from the feed of the antenna should arrive at the targeted plane phase front at the same delay time. The surface contour of the dielectric body, which causes the same delay time for quasi-optical rays, can be given as shown in Eq. 2.4.

$$y(x) = \sqrt{\frac{\varepsilon_r - 1}{\varepsilon_r}} \cdot \sqrt{R^2(\varepsilon_r - 1) + 2Rx - x^2} \qquad \textbf{Eq. 2.4}$$

Here, ε_r is the dielectric constant of the lens material. The equation Eq. 2.4 can be parameterized by the radius R. The parameterization of Eq. 2.4 can be represented as

$$1 = \left(\frac{x - R/\sqrt{\varepsilon_r - 1}}{R/\sqrt{1 - 1/\varepsilon_r}}\right)^2 + \left(\frac{y}{R}\right)^2. \qquad \textbf{Eq. 2.5}$$

This is an ellipse with the semi axes $\boldsymbol{R/\sqrt{1-1/\varepsilon_r}}$ and $\boldsymbol{R}$. If $\boldsymbol{R/\sqrt{1-1/\varepsilon_r}}$ is adjusted along the major axis (X-axis), the feeding point can be placed in the focal point

[11] Pohl, N., "A dielectric lens antenna with enhanced aperture efficiency for industrial radar applications," in *Antennas and Propagation (MECAP), 2010 IEEE Middle East Conference on*, vol., no., pp.1-5, 20-22 Oct. 2010 (doi: 10.1109/MECAP.2010.5724171)

of the ellipse. The ellipsoid is obtained by the rotation of the ellipse around the major axis. The dielectric ellipsoid lens used in the MPR is made from Teflon ($\boldsymbol{\varepsilon_r = 2.08}$).

The largest physical dimension R is around the center point of the ellipsoid. The quasi-optical rays are diffracted at the critical angle of total internal reflection on the dielectric antenna surface. The rays, non-diffracted, are totally reflected and results in evanescent waves on the antenna surface. This fact leads to increase the radiating aperture area, thanks to which there is an increase in the aperture efficiency of the antenna. Additionally, the well tapered radiating field in the aperture plane results in a low side lobe level.

2.5.3. Radiation Pattern

The relevant antenna parameter for the image resolution is the antenna directivity. As discussed earlier it depends on the antenna aperture size. Therefore the two available antennas (R=18 mm and R=37 mm) have been simulated with CST Microwave Studio™ and their 3D radiation patterns are compared in Fig. 2.15. Both antennas lead to a highly focused beam. Sidelobes are mainly present in the *H* plane of the radiated field which corresponds to the xz-plane.

For a more detailed analysis the radiation diagram of both antennas in the xz-plane is shown as a function of the azimuth angle in Fig. 2.15. In the simulation, dielectric losses were not considered, however due to the use of Teflon, assuming low losses seems to be a valid simplification.

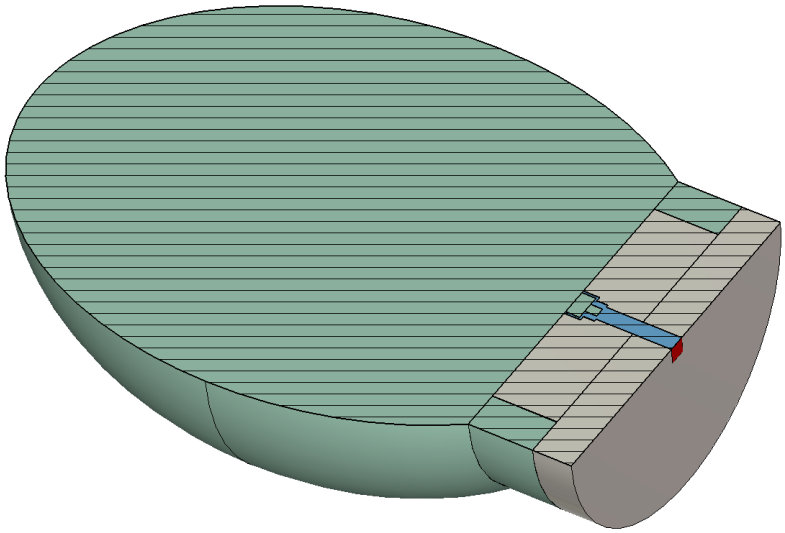

Fig. 2.13: Dielectric Lens Antenna with cutplane

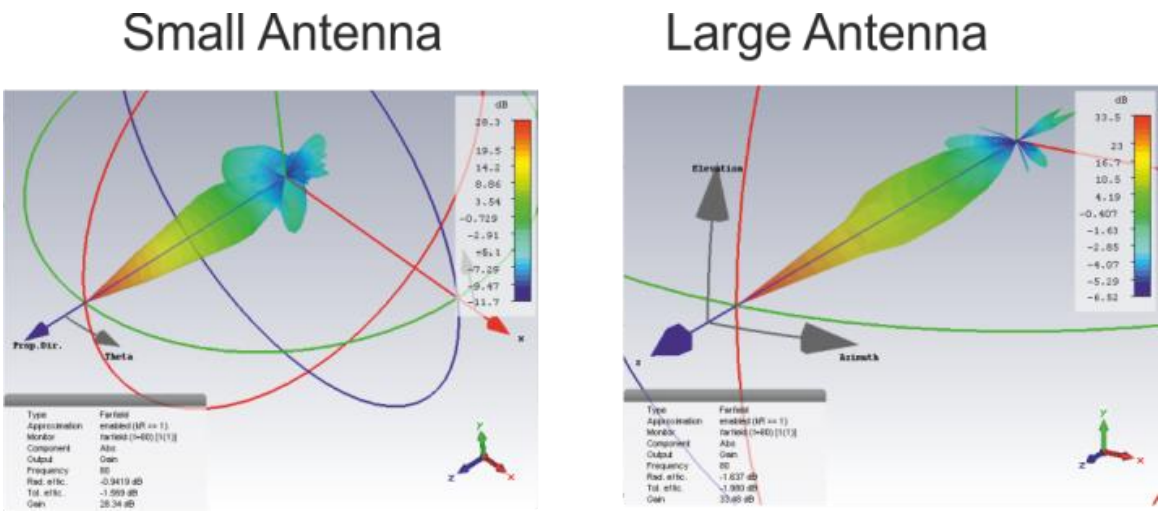

Fig. 2.15: Simulated radiation pattern of large and small aperture dielectric antenna

As shown in Fig. 2.14, the large aperture leads to a simulated antenna gain as high as 33.5 dBi. On the other hand the large electrical size leads to a sidelobe suppression of only 13.5 dB. The 3dB beamwidth of 2.4° promises to enable highly resolved images. The smaller antenna obtains 5.2 dB less gain. The 3dB beamwidth is 4.9° following the results of the simulation. The sidelobe suppression is only slightly enhanced to 14.2 dB, while the separation of the sidelobes from the main lobe is far more significant. From an imaging point of view the larger aperture would be a clearly preferable option. The mechanical point of view will be considered in a later section discussing the MPR realization.

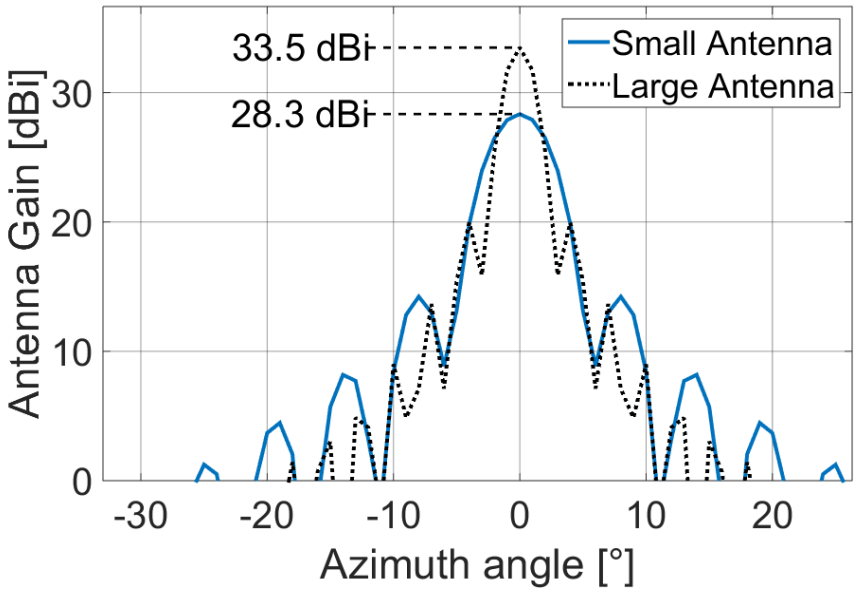

Fig. 2.14: Radiation diagram of small and large dielectric antenna as a function of azimuth angle

2.5.4. Feeding Element and Antenna Realization

The feed of the antenna is a circular waveguide. In order to guide the wave into the dielectric lens body, a stepped impedance transformer is employed. The dimension of the dielectric lens is R=18 mm and R=37mm. For an optimal behavior of the whole antenna, its simulation is performed by CST Microwave Studio. The feeding element should have far field characteristic illuminating electromagnetic waves into the inner part of the antenna below the critical angle of total internal reflection as shown in Fig. 2.16. As mentioned before, the feeding element phase center should be placed on the focus point of the ellipsoid.

The realization of the antenna is shown in Fig. 2.17. The dielectric lens is mounted at the outside of the waveguide, which does not influence the radiation property of the antenna. The dielectric lens is almost independent of frequency but only limited by the antenna feeding element.

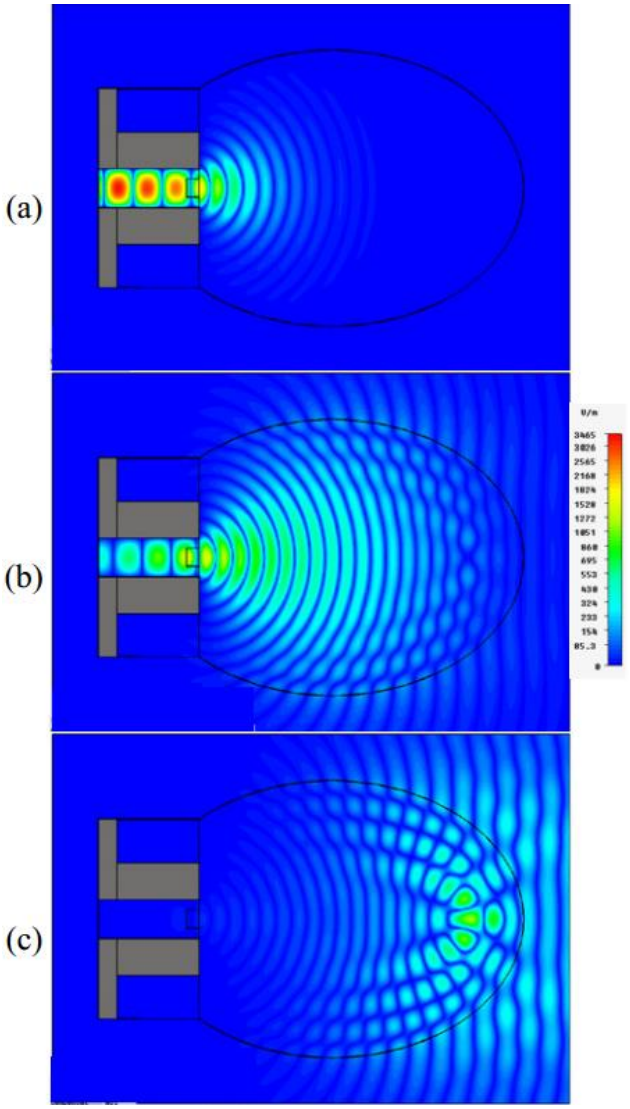

Fig. 2.16: Transient E-field simulation at different time steps.

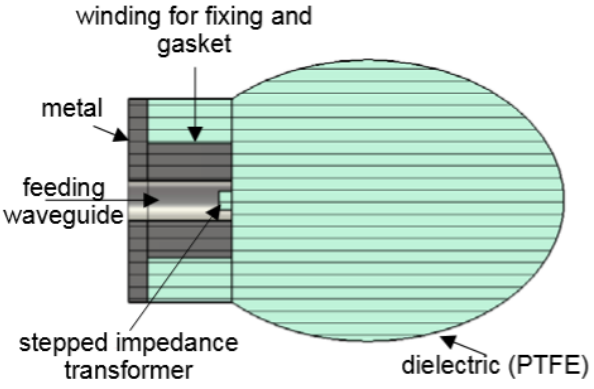

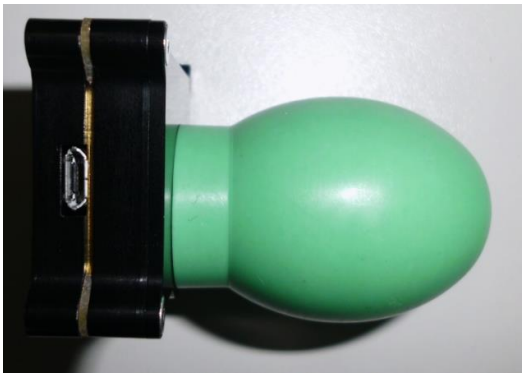

Fig. 2.17: Realized antenna assembly

3. 2D Mechanical Pivoting Radar

The MPR was constructed to provide 2D information about the environment of the constructed vehicle before the MIMO based radar camera is available. This is the main focus of Task 1.1. The following section should give an impression of the structure and performance of the MPR for this task. Beside the radar module described in the last section the development of the imager required a number of other subtasks to deliver usable images in the required format. A mechanical setup was developed to enable mechanical beam steering with sufficient accuracy and resolution. This does not only involve mechanics but also includes electrical interfaces, control circuitry and digital interfaces communicating with modules supplied by other partners. After describing the hardware and its interfaces, image formation algorithms are discussed and demonstrated. This includes the reduction of the 2D images in one-dimensional time-of-flight data sets as well as noise suppression filtering and range gating. The performance of the MPR is demonstrated for different radar bandwidths and aperture sizes. Finally, the software implementation in ROS is presented to provide the required information for integrating the MPR on its robotic platform.

3.1. Concept and Design

The 2D MPR mainly consist of two separate substructures. Firstly, the FMCW radar as described in chapter 2.3 is used and secondly a motor with belonging motor controller for rotating the radar (see Fig. 3.1) has been designed. In order to allow a continuous rotation of the radar along a vertical axis, a slip ring is also required.

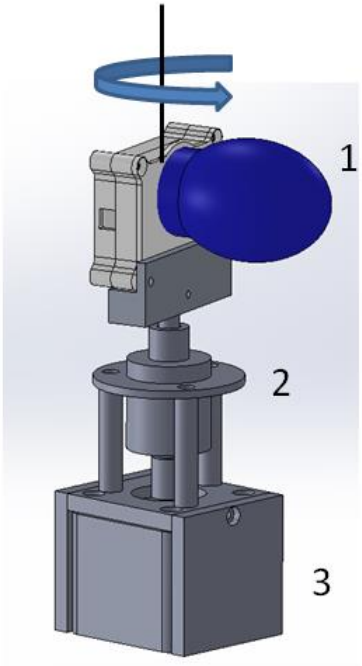

Fig. 3.1: CAD drawing of the mechanical beam steering concept (1 - FMCW radar, 2 - slip ring, 3 - Motor)

While the radar is used for obstacle detection, the motor is required for the mechanical beam steering. A stepper motor was chosen in order to provide a flexible use of the MPR in both, continuous rotation and stepping applications.

In stepped mode, radar measurement and motor movement alternate, so that measurements can be carried out in well-defined positions. Due to the transient movement behavior introduced by interrupting the motor rotation for every acquisition, the scanning frequency is limited in respect of measurements in a given time. In contrast to this the continuous mode can reach higher scanning frequencies. Here measurements are carried out, while the motor is rotating with constant speed. Therefore the delay between the measurements can be reduced. The disadvantage of this approach is the fact, that radar measurements are not carried out at particular positions, but rather during an angular movement, which is determined by the speed of rotation and the sweep time of the FMCW radar. Depending on the circumstances, this can lead to degraded image quality, therefore the correct mode with respect to the application at hand has been chosen.

In order to allow sufficient scan rates for 360° measurements in continuous mode, a rotation speed of at least one round per second should be achieved. In respect to this requirement a stepper motor and motor controller have been chosen. The used stepping motor controller for managing the mechanical beam steering has the ability to control two stepper motors separately both in position and speed. Therefore the controller can be used for the 2D MPR as well as for the 3D MPR (see chapter 4). This has the advantage that main parts of the design can be reused in a later stage of the Task. The control unit supports the rotation of the motors in steps as well as in a continuous rotation with a certain, given velocity. This offers the possibility to implement both described scanning methods without use of additional hardware or software. For communication with the motor controller an RS232 interface is used, which is a well-known and robust interface, suitable for interfacing from either MATLAB or C/C++.

The chassis of the MPR primarily consist of a ground plate and a top plate with the electrical interface integrated. Both plates are connected by an aluminium beam. In consequence this profile appears in every 360° measurement as a fixed target. While this may seem to be a disadvantage, it is in fact used for data alignment in the imaging process. The main idea is that in one 360° acquisition, this fixed target can be easily distinguished in the data such that it can be used as a reference in the coordinate system.

The power supply of the MPR should use common DC voltages, so that the MPR can be used without much effort by using a standard laboratory power supply as well as a battery power supply when mounted on the robot. For supplying the FMCW radar module with power, two different methods are possible. Depending on the chosen method only one voltage or in maximum two voltages are needed for supplying power the MPR.

In order to protect the mechanics and the radar module from rough environment conditions, but also to avoid injuries when the MPR is being operated, a radome has been integrated into the overall design. Additionally we want to emphasize that the device shall never be operated without the radome being mounted. The material of the radome has to be as transparent as possible for the used frequency range of the FMCW radar and the shape should be optimized for low reflections. Further investigation has been done in section 3.2.5.

3.2. Implementation

The implementation of the 2D MPR concept described in section 3.1 can be seen in Fig. 3.2. In these CAD drawings the radome is not shown in order to provide a look at the internal elements. In addition, the wiring of the components is also hidden in this figure.

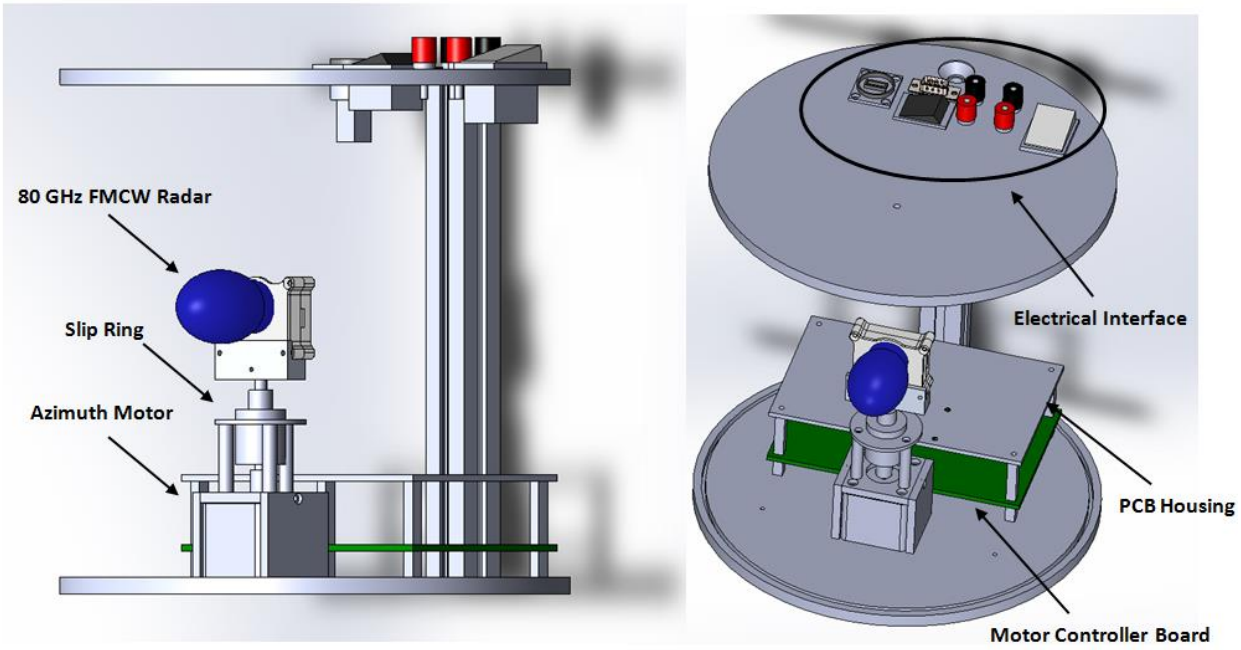

Fig. 3.2: CAD drawings of the 2D MPR

Before describing the components and their functions in detail, an overview about the wiring and the relation between the components will be given. In Fig. 3.3 the circuit and signal flow diagram of the 2D MPR is shown. With regard to the voltage supply of the MPR the typical values are shown.

On the left side of the diagram the electrical interface can be seen (marked in red). This part will be explained separately in section 3.3. For supplying power to the MPR, normally two different voltages need to be applied. One voltage input is used for the power of the motor and the other one for supplying the motor controller. The latter has a power switch included, which can be used for turning the MPR on or off. In fact, this switch only disconnects the power from the controller itself, which in turn shuts the motor current regulation off. Therefore the power supply current to the second power supply input drops to zero as well.

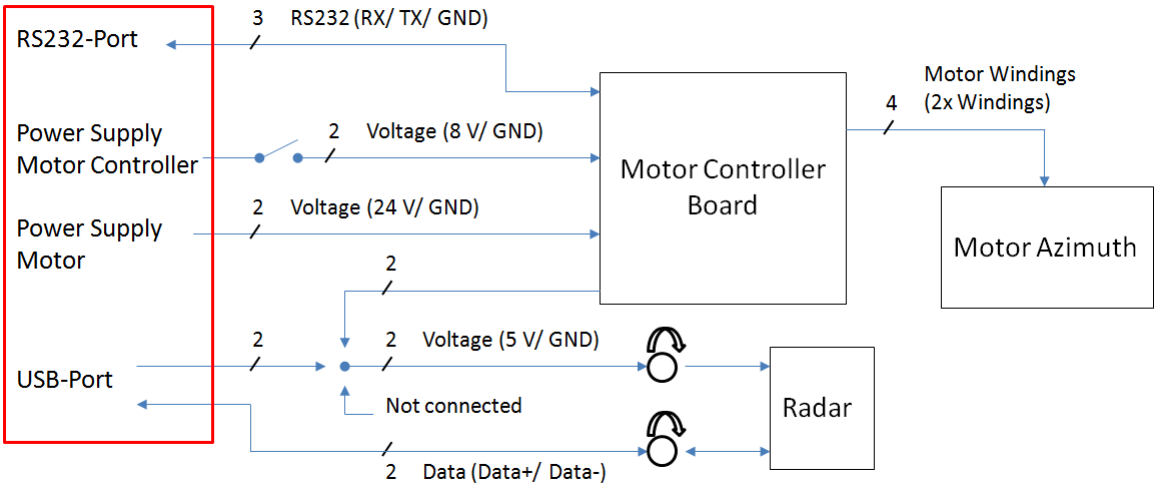

Fig. 3.3: Circuit and signal flow diagram of the 2D MPR

The FMCW radar module is supplied with power using its USB 2.0 interface. Since the power consumption of the radar exceeds the USB 2.0 specifications slightly (see section 3.4), it is not guaranteed that the radar operates in a stable mode under all circumstances, especially when the PC controlling the MPR has to power further USB devices or a long USB cable is being used. Therefore the radar can optionally be powered by the motor controller board instead of the USB Interface of the MPR. In order to choose which power supply input will be used, a rocker switch with three positions is integrated into the power line of the radar (as outlined in Fig. 3.4). Two of the positions are used for choosing the power source and the third for turning off the radar. The latter is necessary, because if the radar power is provided by the USB interface, the radar would still be active, even when the MPR turned off with its power switch.

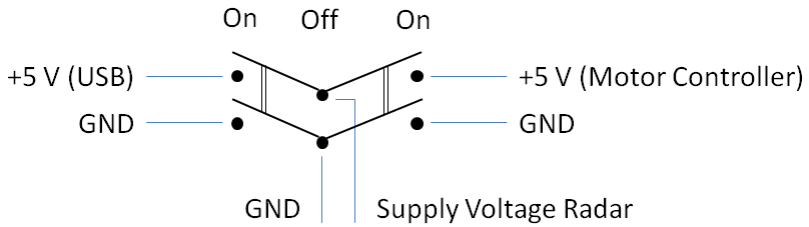

Fig. 3.4: Switch function of radar switch

The connection of the power and USB data lines between electrical interface of the MPR and radar is done by the use of a slip ring. The slip ring allows transmitting these signals even while the radar is rotating continuously. Otherwise the rotation would be limited by the length of the used cables.

For communication with the motor controller a simple RS232 interface is used. The three required wires for transmit data, receive data and ground are connected directly to a male DSUB-9 connector.

Besides the described signals above, there are four additional lines. These connect the motor controller with the windings of the stepper motor.

Following this brief overview, now the focus will move on to the particular components of the MPR. Beginning with the radar module, the other elements will be described from top to bottom, thus following the mechanical connection between the components.

3.2.1. 80 GHz FMCW Radar Module

In this section, only the information required for the MPR implementation is summarized. Although the use of different antennas (see section 3.6.1) and backends is possible, the details shown in this section are restricted to the radar module as it has been finally applied in the MPR. Within the following illustrations, the radar module and the antenna will be considered as one unit, when talking about the radar module.

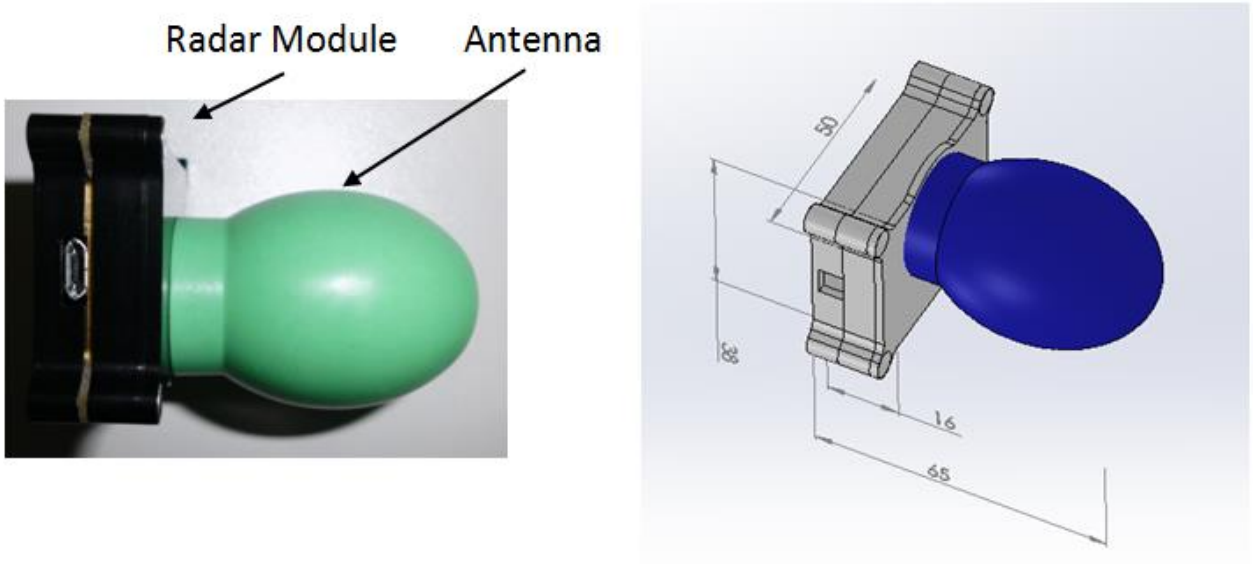

Fig. 3.5: Photograph and CAD drawing (in mm) of the 80 GHz FMCW radar module

As shown in Fig. 3.5, the radar's outline amounts to 50 x 38 x 65 mm (W x H x L). The weight roughly amounts to 145 g, whereas 75 g result from the antenna. These specifications will be important for the choice of the motor.

As mentioned before, communication and power supply of the radar are realized via an USB 2.0 interface, which is implemented as a micro USB connector. The required electrical power is about 3 W (600 mA at 5 V) and has to be considered in respect to the slip ring. A USB data rate of up to 16 Mbit/s, when transmitting the digitized IF signal, also has an influence on the choice of the slip ring. Apart from transmitting the measured IF signal, the parameterisation of the radar is also done via the USB interface.

The connection between radar and slip ring is done by the use of an angled micro USB connector (see Fig. 3.6) in order to reduce the wire length between the radar and the slip ring as much as possible. Therefore the vulnerability against electromagnetic disturbances is reduced. Additionally the moment of inertia will be

lower, so that any mechanical stress on the connection due to a high rotation speed will also be lower.

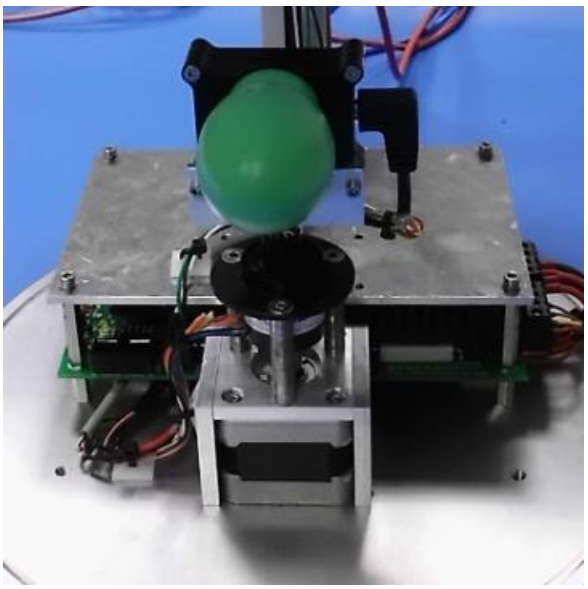

Fig. 3.6: FMCW radar mounted on stepper motor and slip ring

3.2.2. Slip Ring

The slip ring has the function of transmitting power and data signals from the stationary MPR body to the rotating radar. The following requirements were demanded during the concept phase:

- At least four rings for the support of the radar interface (+5 V, GND, Data+ and Data-)
- At least a current of 600 mA per ring to supply the radar
- Data transmission with the USB 2.0 standard must be possible
- A rotating speed of at least 60 rounds per minute, enabling a high acquisition speed

Besides these main tasks a hollow shaft for the slip ring is desirable. This implementation allows a lower height of the MPR in comparison to a slip ring with a solid shaft. The latter would have to be placed above the radar, whereas the combination of hollow shaft and motor shaft results in a much lower profile height. Taking into account these requirements, a slip ring from the rotarX serie from B-COMMAND GmbH was chosen for the MPR. As seen in Fig. 3.7 (right), the slip ring meets all demands and in addition has enough headroom for future changes.

Based on these specifications, two separate rings for power supplying the radar (+5 V and GND) would be sufficient. Nevertheless it was decided to use four rings for the power lines (two rings with +5 V and two rings with GND) in order to reduce any potential voltage losses due to the ring contacts. When supplying power to the radar module by using the motor controller board, this might not be critical, however when using the USB interface of the MPR, it may prove helpful. The two data lines of the USB

Electrical and mechanical specifications	
Number of rings	12
Current	2 A per ring
Mechanical Angle of rotation	360° continuous
Rotating speed (max.)	200 rpm

Fig. 3.7: Slip Ring RS-HX2512-002 and its specifications

interface are connected to one ring each. In order to reduce electromagnetic disturbance, the wires corresponding to these rings have been twisted. The slip ring itself is mounted on the motor using distance bolts (see Fig. 3.6).

3.2.3. Stepper Motor

For the purpose of making a rough assessment of the required motor torque, the radar module incl. antenna flange and antenna have been modelled as two point masses at their respective balance points (see Fig. 3.8).Here, BP1 represents the balance point of the radar module and flange and BP2 the balance point of the antenna. The distances (in mm) of these points to the assumed axis of rotation are also shown.

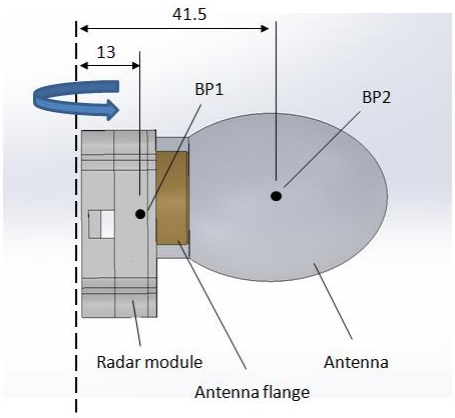

Fig. 3.8: Balance points of radar module and antenna

For this simple model the moment of inertia was estimated. For a point mass with the weight **m** and distance **r** to an axis of rotation the moment of inertia **I** is estimated by the following equitation.

$$I = m * r^2$$

By the use of the parallel axis theorem the moment of inertia for the comprehensive model is given by:

$$I = m_{radar} * {r_{radar}}^2 + {m_{antenna} + r_{antenna}}^2$$

With the values from section 3.2.1 and Fig. 3.8 the moment of inertia amounts to 0.000141 kgm².

During the concept phase it was considered, that the maximal speed of rotation would be 300 rounds per minute (5 Hz)[12]. Higher speeds seemed not to be necessary, because otherwise the angular resolution of the radar measurements would have become too low. The time for accelerating from standstill to maximum speed was estimated to one second.

Under these aspects, the minimal torque moment **τ** was calculated by the following equitation.

$$\tau = I * \alpha$$

The angular acceleration α was assumed to be constant. Therefore α has been calculated to be about 31.5 s^{-2} with respect to the maximum angular velocity.

$$\propto = \frac{d\omega}{dt} = \frac{5 * 2\pi/s}{1s} \approx 31.5\ s^{-2}$$

Therefore the estimated minimal motor torque is 0.44 mNm.

$$\tau = I * \alpha = 0.000141\ kgm^2 * 31.5\ s^{-2} = 0.44\ mNm$$

Since there are no external forces, which affect the motor additionally, a quite small stepper motor is sufficient. To allow for some headroom, for applying larger antennas or additional mechanics for example, a stepper motor with a holding torque of 25 Ncm at maximum power has been chosen (see Fig. 3.9). Since the required motor torque is much smaller, the constant motor current can be set to a comparatively small value. While operating the MPR, the motor current is set to 50 mA at a motor voltage of 24 V.

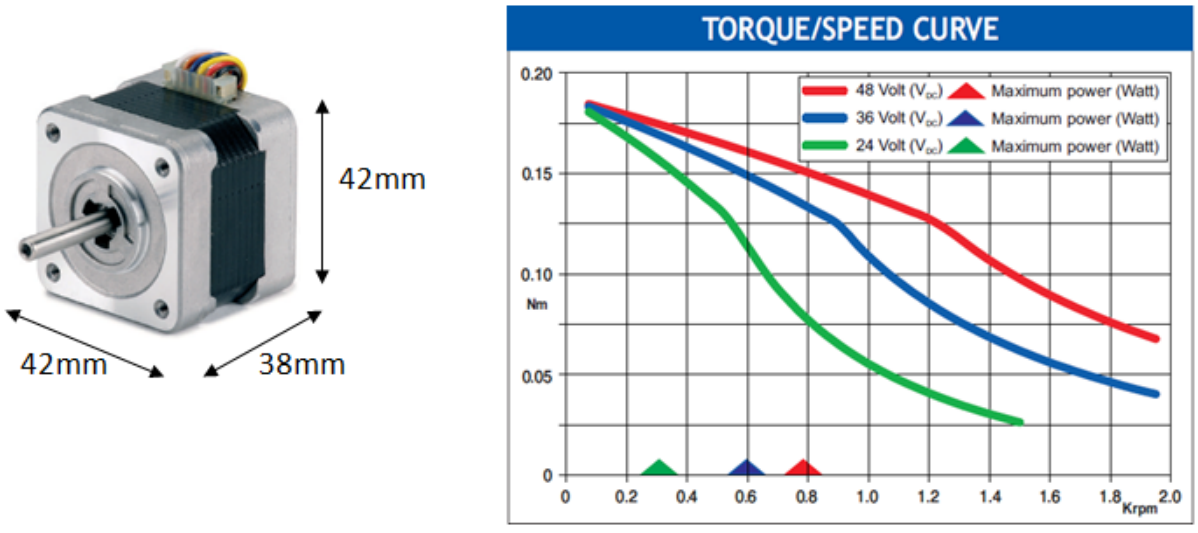

Fig. 3.9: Outline dimensions and torque/speed diagram of 2D MPR stepper motors

[12] Eventually, the max. rotational speed of the MPR was limited to 200rpm by the slipring.

The motor supports a basic step angle of 1.8° in full step mode. When operated in half step mode, the step angle is correspondingly 0.9°. By these angles the angular resolution for each possible measurement position can be determined.

Since the motor is operated in a bipolar fashion, the center taps of its windings are not used, thus the motor is connected to the motor controller board (described in the next section) with four wires. Due to the motor shaft being too short for applying the radar as well as the slip ring, a shaft extension has been used.

3.2.4. Motor Controller Board

For operating the stepper motor, a motor controller board (RN-Schrittmotor Version 1.7) from Robotikhardware has been used (see Fig. 3.10). This board offers all the required features, which were considered in the concept phase. The implemented hardware and firmware of the controller allow controlling up to two step motors - each of them independently, if needed. It is compatible to most of the stepper motors available on the market. Therefore the controller board is a suitable choice for both the 2D MPR (and the 3D MPR) design. Besides controlling and powering the applied motors, additional devices can also be powered by the controller board. Though this is limited to a supply voltage of 5 V, it satisfies the requirement of the radar module. Due to the fact that the supply voltage on this output is generated by a fixed voltage regulator from the actual motor controller supply voltage, the separation of controller supply voltage and motor supply voltage is useful. This way, the supply voltage applied to the stepper motors can be set to a higher voltage level, allowing the required motor current to be reduced. This might be necessary in respect to the required mechanical power and maximum allowed motor current. Additionally the power supply voltage for the motor

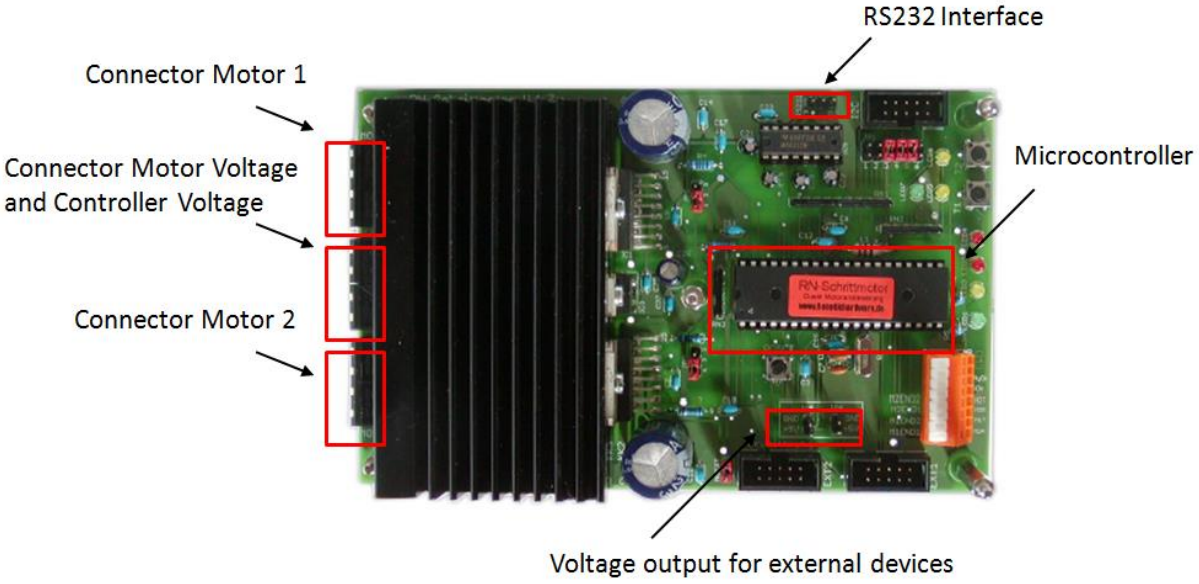

Fig. 3.10: Motor Controller Board

controller can be reduced in order to limit heat dissipation by the fixed voltage regulator, in case the radar module is powered by the motor controller board. However, if the radar module is powered via the USB interface, it is not mandatory to use different voltage levels for supplying the MPR. In this case it is possible to connect both voltages to a single supply voltage.

The main functionality of the motor controller board is implemented in the supplied microcontroller. It is responsible for controlling the motor positions and speeds as well as the communication using the RS232 interface. The firmware enables the user to set the motor parameters for the respective application. After defining parameters as needed, the motors can be controlled either by specifying a number of steps or the speed of rotation to allow continuous rotation of the motor. In case of the 2D MPR, the parameters and commands listed in Table 3.1 are used to control the motors.

Command/ Parameter	Comment
Set motor current	The motor current is defined by this parameter. It can be changed, though the motor is moving. By adjusting this value, the engine power can adapted with regard to the actual circumstances (a higher engine power while accelerating and a lower one after final speed is reached).
Set step mode	The motor controller supports full step mode as well as half step mode.
Activate/ Disable motor output stage	---
Set direction of rotation	In the 2D MPR the motor rotates always to the right (clockwise)
Set velocity	Speed of rotation is defined by this parameter. In respect to the stepped measurement mode, the velocity normally can be neglected. But in continuous measurement mode the angular resolution essential depends on speed of rotation.
Set acceleration	This parameter defines acceleration for reaching final motor speed.
Start continuous rotation	---
Move particular steps	The motor will move the given steps. The actual moved angle depends on the step mode (the angle doubles, if the mode is full step in compare to half step mode.

Table 3.1: Used commands and parameters of the motor controller

3.2.5. Radome

In order to protect the mechanics and radar module from the outside environment, a radome has been designed. However the radome must not disturb the radar measurements. For choosing a suitable material for the radome, experiences from other applications have been used. In general high density polyethylene based plastics (HDPE) have shown good electromagnetic transmission characteristics for frequencies used by the MPR radar. In addition, mechanical processing of PE sheets is possible with little effort. The radome has been designed by using a sheet of HDPE which is bent around the outer perimeter of the MPR. This has the benefit, that independent from the field of view of the radar only few reflections from the radome will actually be picked up by the radar module, instead a high percentage of the actual lost transmitted power is diffusely reflected within the radome.

In order to give the radome its ring-shape and to allow easy mounting on the MPR, a circumferential slot has been used in the top and the bottom of the MPR chassis.

In these slots a PE HD sheet with a wall thickness of 2 mm has been fixed. At the rear of the MPR, the HDPE sheet is screwed to the aluminum-profile. The mounted radome can be seen in Fig. 3.12.

3.2.6. Fully Integrated MPR

The 2D MPR has mount points at the top and bottom side. At the bottom there are four threaded holes (M5), which can be used for mounting the MPR on a robot or in other systems. Additionally, another threaded hole (M5) has been added to allow mounting additional devices on top of the MPR. It is located on the radar module's axis of rotation. This allows additional devices to be mounted to the MPR that need to operate on the same rotational axis as the MPR.

The fully integrated 2D MPR has an outer diameter of 250 mm and a height of 256 mm not accounting for the connectors at the top and about 275 mm including the connectors. The overall weight amounts to about 3.4 kg. The following photographs give an impression on what the fully assembled MPR looks like with (Fig. 3.11) and without the radome (Fig. 3.12) mounted.

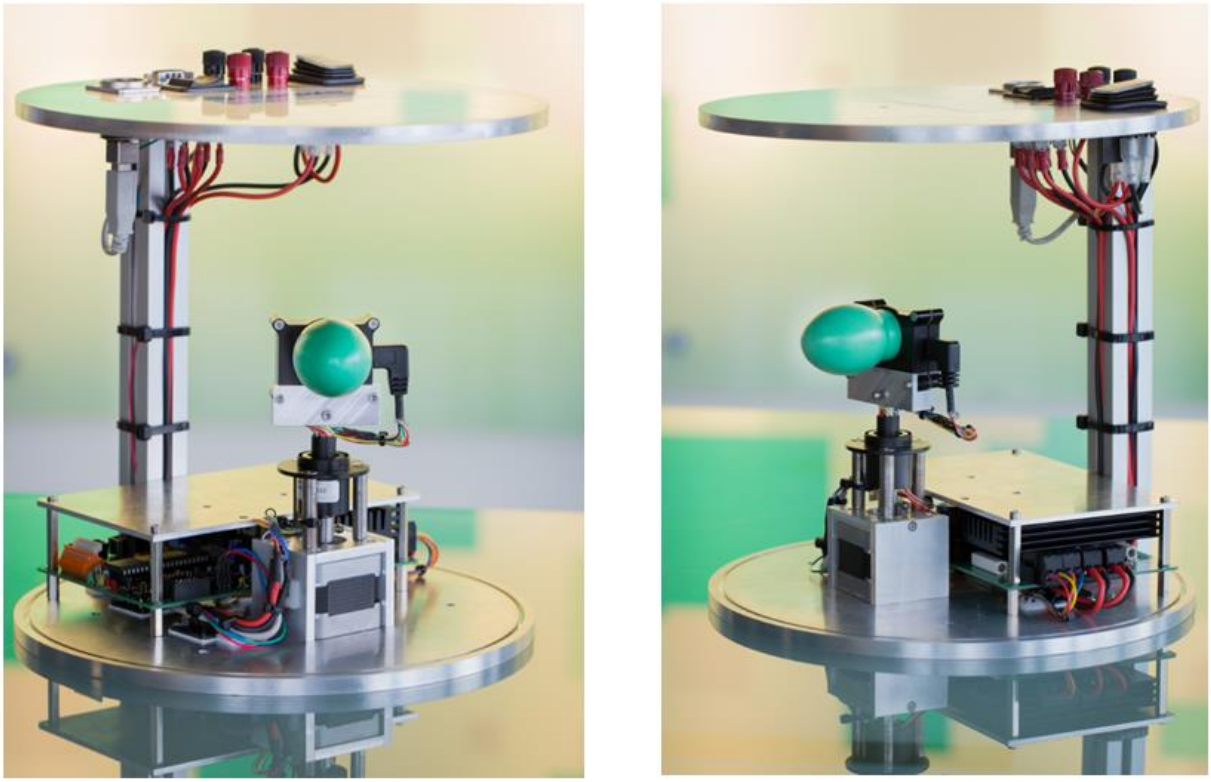

Fig. 3.11: Photographs of the 2D MPR

Fig. 3.12: Photograph of 2D MPR with mounted radome

3.3. Electrical Interface

After describing the implementation of the 2D MPR, the electrical interface is introduced. All required mechanical and electrical interfaces can be found on the top of the module as shown in Fig. 3.13.

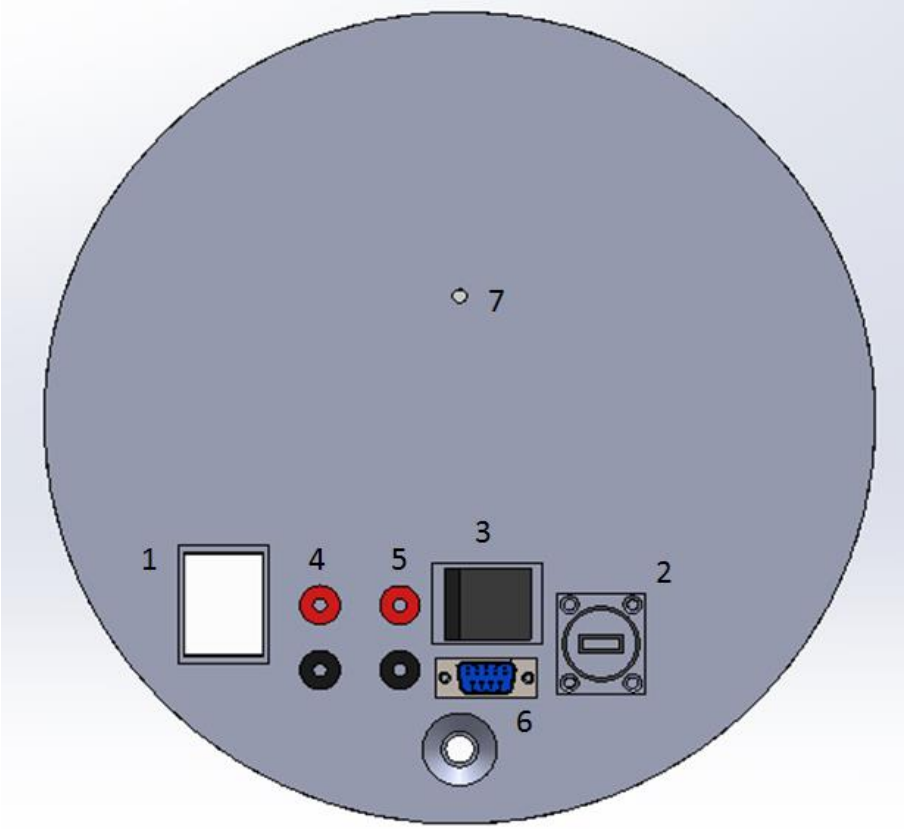

Fig. 3.13: Interface of the MPR (top view)

The following table provides a brief description of all interfaces to ease the integration in a complete sensor suite. Further information can be found in the sections before.

Pos	Function
1	Power On/Off: This switch is used for turning the MPR on or off. Attention: If the power supply of the radar is provided by the USB interface (Radar switch (Pos 3) in position I), the radar is still active, even when MPR is turned off.
2	USB-Interface (2.0): Communication interface of the radar.
3	Radar switch: The power for the radar can be supplied either by the USB-interface (Pos 2) or by the motor controller board. For the latter case, the required 5V supply voltage is generated on the controller board from the controller supply voltage (Pos 4) with a fixed voltage regulator. The radar switch has the following states: Switch position I: Supply voltage for the radar provided from the USB-interface. Switch position 0: The radar is turned off. Switch position II: Supply voltage for the radar provided from the motor controller board.
4	Supply voltage for motor controller board: The supply voltage for the motor controller board can be chosen within a voltage range between 8 V (DC) and 24 V (DC). If the radar is supplied by the motor controller board, the input voltage should not exceed 12 V (typ. 8V) in order to reduce the thermal power dissipated. When the supply voltage for the radar is provided by the USB-interface, then 24 V can be applied. By doing this, it is possible to connect motor controller voltage (Pos 4) and motor voltage (Pos 5) in parallel. The current consumption of this voltage input is about 70 mA or about 700 mA if the radar is also supplied by the motor controller board
5	Supply voltage for stepper motor: 24 V (DC) While accelerating the motor after start, the current consumption is about 400 mA. When final speed is reached (after 5 seconds) the current consumption is reduced to approximately 70 mA.
6	Communication interface for the motor controller: Serial interface (RS232). This interface needs a 9 pole serial cable (RX and TX must not be crossed).
7	Mounting option for additional devices: The threaded hole (M5) is located at the axis of rotation of the radar.

Table 3.2: Interface of the MPR

It should be noted that a summarized version of the electrical interface description can be found in the appendix 8.1.

3.4. **MPR Specifications**

		Min	Typ	Max	Unit	Remarks
Electrical System Specifications						
	Supply Voltage Motor Controller	7	24	24	Volt	If 80 GHz Radar is supplied via motor controller, then less than 12 V
	Supply Voltage Motor	7	24	30	Volt	At least 24V is needed to ensure sufficient torsional moment
	Supply Voltage Radar	4.5	5.0	5.5	Volt	USB Powered
	Supply Current Radar		600		mA	Exceeds USB 2.0 Spec
Azimuth Motor Currents						
	Initial Current		300		mA	While initializing and accelerating motor (about 5 sec.)
	Motor Current		50		mA	In normal operation
Mechanical Specification (Azimuth)						
	Movement Range		360		Deg	Continuous
	Speed of Rotation*		2.5		Hz	Continuous
	Movement Resolution* Continuous		1.8		Deg	
	Movement Resolution Stepped mode		1.8		Deg	(full step)
	Movement Resolution Stepped mode		0.9		Deg	(half step)
Acquisition Specifications						
	Ramp Repetition Time*		2		ms	1 ms Sweep Time
	Acq. Per Revolution*		200			At 2.5 Hz Rotation Rate
	Update Rate		2.4		Hz	Continuous
	Range Resolution*		3.75		cm	
	Minimum Range*		0.2		m	Referenced on axis of rotation
	Maximum Range*		15		m	Referenced on axis of rotation
Mechanical Outline Dimensions						
	Diameter		250		mm	
	Height		275		mm	Without electrical interface 256 mm
	Weight		3.4		kg	
Parameters marked with * can be adjusted						

3.5. **Image Formation Algorithm**

This chapter describes the rotation, the angular resolution for both modes as well how the radar data is measured and processed. At first the used rotation axis should be described.

The rotation of a rigid object around a stationary axis A as shown in section 3.1 is determined by the angle of rotation φ (see Fig. 3.14) as a function of time. For this function, the angular velocity $\omega = \dot{\varphi}$ and the angular acceleration $\alpha = \dot{\omega} = \ddot{\varphi}$ can be derived. The angular velocity and the angular acceleration are vectorial values, which are oriented in parallel in relation to the spatially-fixed rotation axis.

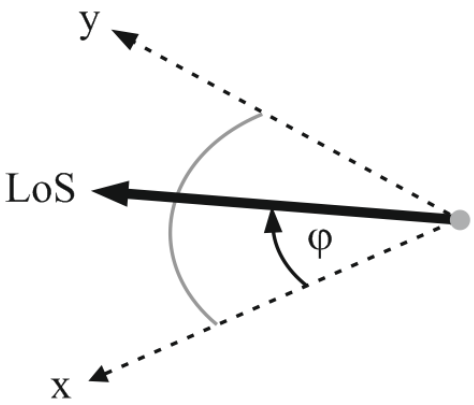

Fig. 3.14: Angle of rotation (Top View)

Concerning the Radar, the rotational axis is located at the center of the motor shaft. The direction of rotation is clockwise and the rotation mode of the MPR can be chosen between continuous or stepped mode.

Additionally, the angular resolution differs for the two different modes, continuous or stepped mode. Firstly, the angular resolution for the stepped mode is described. For this case full step mode and half step mode (see Table 3.2) are possible. These two modes are adjustable before performing the measurements and the angular resolution $\Delta\varphi$ for the motor can be 1.8° (full step mode) or 0.9° (half step mode).

Using the continuous mode, the angular resolution is depending on the ramp duration T_{sweep}, the pause duration T_{pause} (Fig. 3.15) and the angular velocity ω.

The angular resolution for the continuous mode can be calculated with:

$$\Delta\varphi = \frac{U}{n} \qquad \textbf{Eq. 3.1}$$

U is one revolution in ° and n is the number of measurement, which can be calculated with:

$$n = \frac{\omega}{T_{sweep} + T_{pause}} \qquad \textbf{Eq. 3.2}$$

In consideration of the default parameters for the continuous mode, the number of measurements n is equal to

$$n = \frac{2.5Hz}{1ms + 1ms} = 200$$

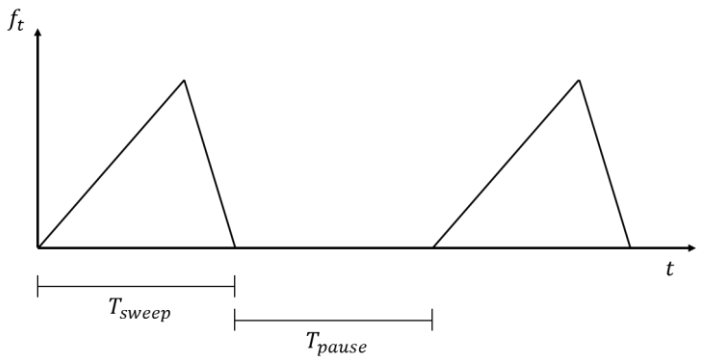

Fig. 3.15: FMCW pulse repetition

Thus an angular resolution of

$$\Delta\varphi = \frac{360°}{200} = 1.8°$$

can be achieved. The values for T_{sweep}, T_{pause} as well as ω are variable.

In Fig. 3.16 a program flow chart of the MATLAB processing script is shown. In the following, the description of the process steps will be illustrated in detail.

The script is divided into several functions. At start-up the system is initialized and the operation mode is chosen. Subsequently, the signal is measured for every angular position and the intensity of every range profile as well as the range data is processed using MATLAB. In the following, the different process steps will be described.

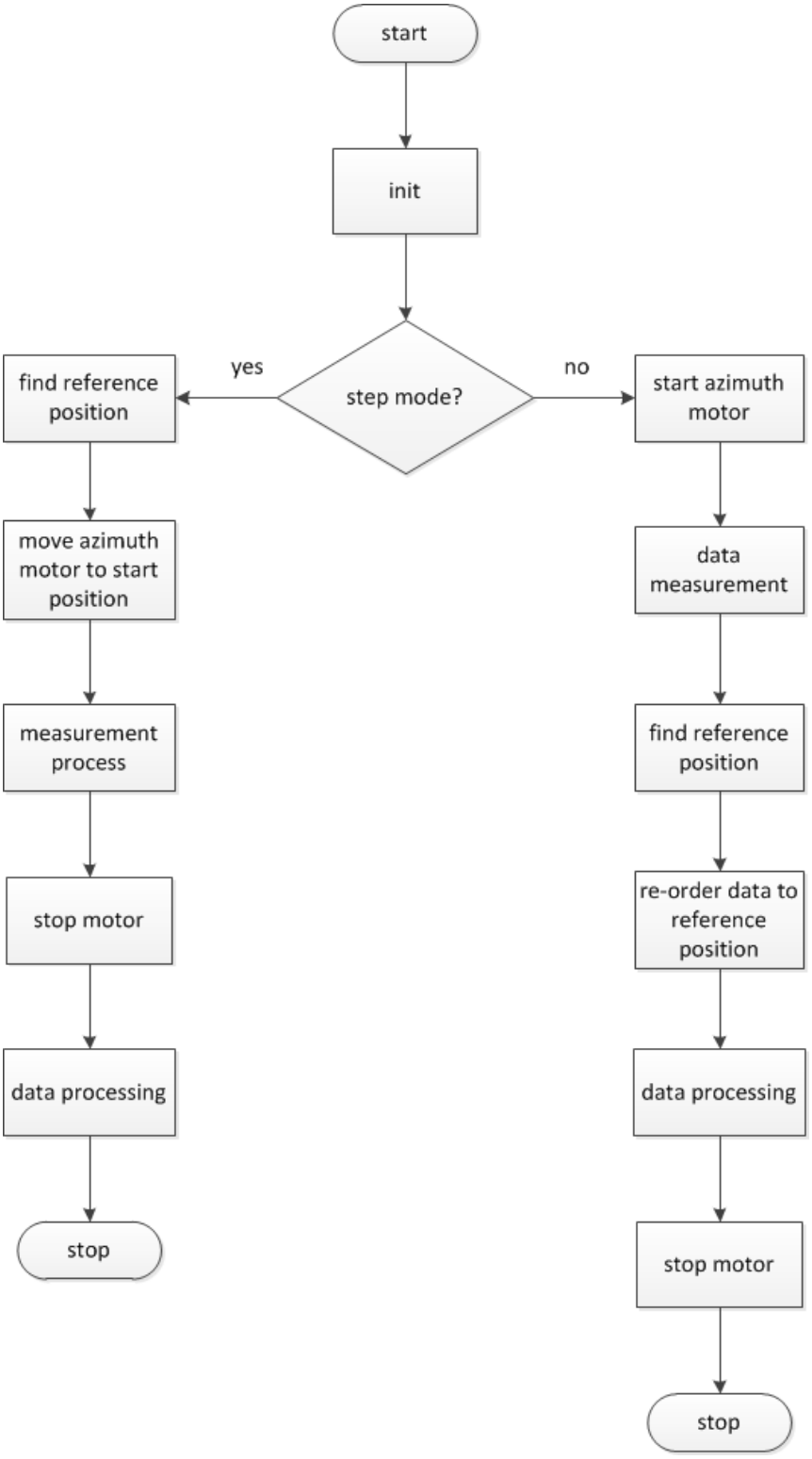

Fig. 3.16: Program Flow Chart

After the start-up the script performs the following initialization steps:

- Initialize COM port for Radar and Motor
- Initialize start and stop for the azimuth angle
- Initialize FMCW ramp parameter for the radar module (this includes the start and stop frequency, the bandwidth and the ramp duration)
- Initialize gain of IF amplifiers
- Initialize RS-232 interface
- Set radar's ramp parameters
- Set motor parameters (this includes rotation direction, velocity, motor current and step mode)

Subsequently, stepped mode or continuous mode can be chosen by the operator. If the stepped mode is chosen, the next step is to find the reference position by performing a whole 360° measurement and evaluate the highest intensity to find the reference position. Afterwards, the radar is moved to the start position and the measurement can be executed. For every angular position the range and the intensity values are received.

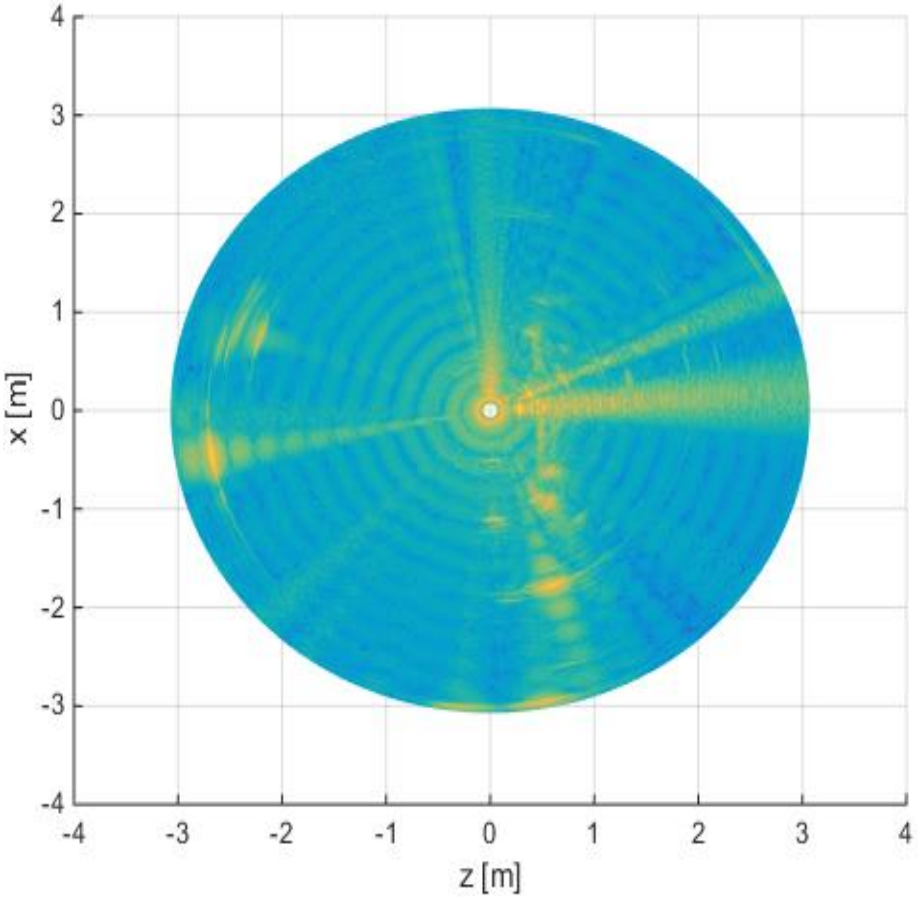

Fig. 3.17: MPR Plot Example

Afterwards, the motor is stopped and the data is ready for the data processing. The collected data has to be mapped from polar to Cartesian coordinates. The polar

coordinates r and θ can be converted to the Cartesian coordinates x and y by using the trigonometric functions sine and cosine:

$$x = r \cdot \cos(\theta) \quad \textbf{Eq. 3.3}$$

$$y = r \cdot \sin(\theta) \quad \textbf{Eq. 3.4}$$

After mapping polar coordinates to Cartesian coordinates, the data is plotted. This plot is shown by an example in Fig. 3.17.

To calculate the correct range to the corresponding bins, the following formula is used.

$$r = \frac{c_0}{2 \cdot BW} \cdot \frac{N_{fft}}{2} \quad \textbf{Eq. 3.5}$$

Where c_0 is the speed of light in vacuum, BW is the Bandwidth of the radar and N_{fft} is the number of bins from the FFT, which can be calculated using Eq. 3.6.

$$N_{fft} = T_{sweep} \cdot F_{sample} \quad \textbf{Eq. 3.6}$$

In case the continuous mode is chosen, the azimuth motor is started and after the motor reaches its target angular velocity, the motor current is reduced and the measurement for a complete 360° rotation can be performed. To allocate the range data to the corresponding angular data, it has to be re-ordered to the fixed reference position. In order to find the reference position, the range data is searched using a range window corresponding to the known distance to the reference position. Once the start position is found, the data is rotated with respect to this location. For further processing, the data is normalized to the maximum value in every angular position. Lastly, the processed data is plotted and the motor stops.

3.6. Experimental Evaluation of the 2D MPR

For evaluating the imaging capabilities of the MPR system, the most relevant test scenario employs an experimental measurement in an environment close to the desired application scenario. In this case an indoor measurement was performed. As shown in Fig. 3.19, two main objects were used. Fig. 3.18 shows their position within the room which was 10 m in length and 4 m in width. The MPR was placed directly in front of a side wall 3 m from the front entrance. The used MPR is capable of moving in elevation and azimuth to enable 3D imaging. However, in the case of this experimental investigation only one motor stage was used controlling the azimuth orientation angle of the antenna. The motor stage as well as the radar module was controlled using the common serial interface of the MPR.

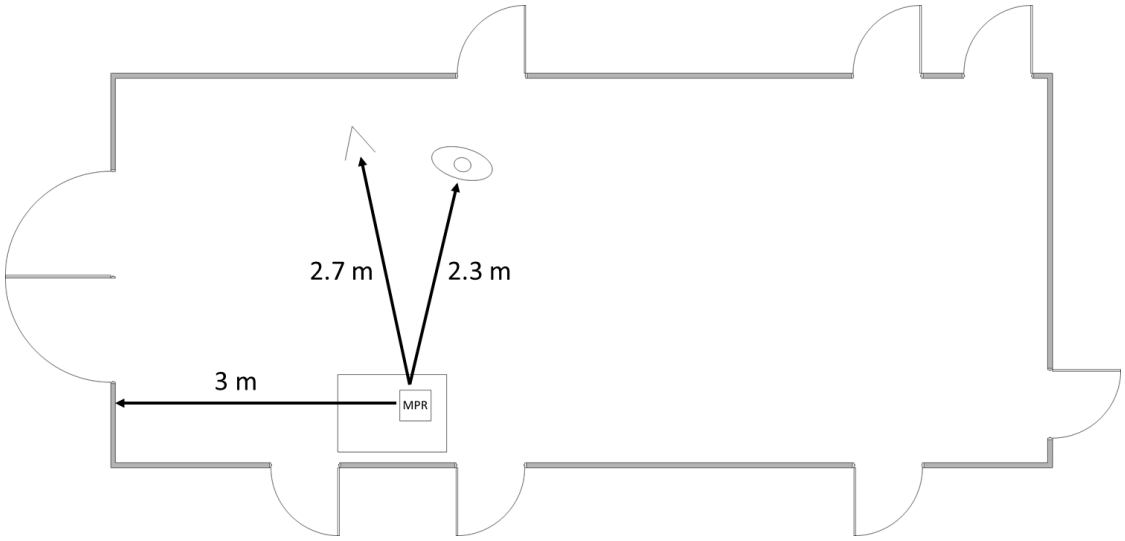

Fig. 3.18: Outline of indoor measurement site

For the characterisation of the radar a trihedral reflector was placed with 2.7 meters distance at an azimuth angle of -10° in front of the MPR. This provided a strong reflection at a closely defined point in space which can be seen as a dirac impulse in the spatial domain. It is very useful for system calibration purposes as well as for characterising the point spread function of the MPR. To get closer to the desired application a person model made out of polymer was taken in order to show the performance of the MPR for more complex objects.

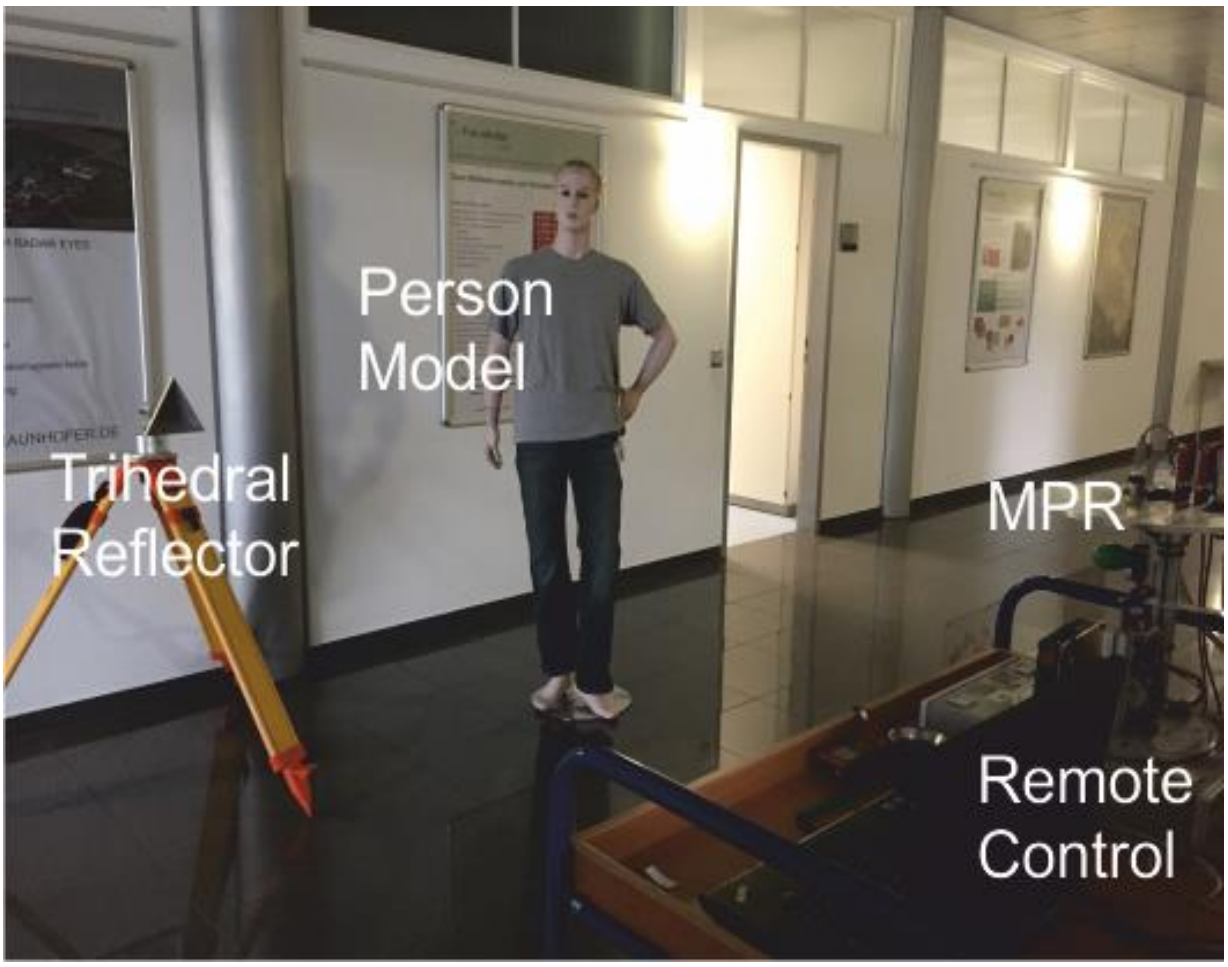

Fig. 3.19: Measurement scene for experimental MPR characterization

3.6.1. Comparison of different Antenna Aperture sizes

As discussed in section 2.5.1 the size of the antenna is crucial for the radar image resolution in elevation and azimuth. The dielectric lens antenna used for the MPR is available in two versions. Both are fed by a WR-10 waveguide connector and are therefore compatible with the developed radar module. The larger antenna shown in Fig. 3.21 is mechanically challenging due to its size and weight. Within the package size chosen for the MPR a movement of this antenna is only possible in the azimuthal direction.

For stable operation on a moving platform, additional mechanical support would be needed since only fixing it with the waveguide flange does not lead to the required stability. Additionally a 360° movement in azimuth is hard to obtain. From a mechanical point of view a smaller antenna aperture is far more elegant to handle. As shown in Fig. 3.21, the size of the smaller version of the dielectric antenna is within the same region as the radar module. It is sufficiently stable by just fixing it using the WR-10 flange and a movement range in azimuth and elevation is possible. The experimental setup of comparing the antennas has led to the decision to use the smaller antenna size for use in the MPR, although it's inferior RF performance.

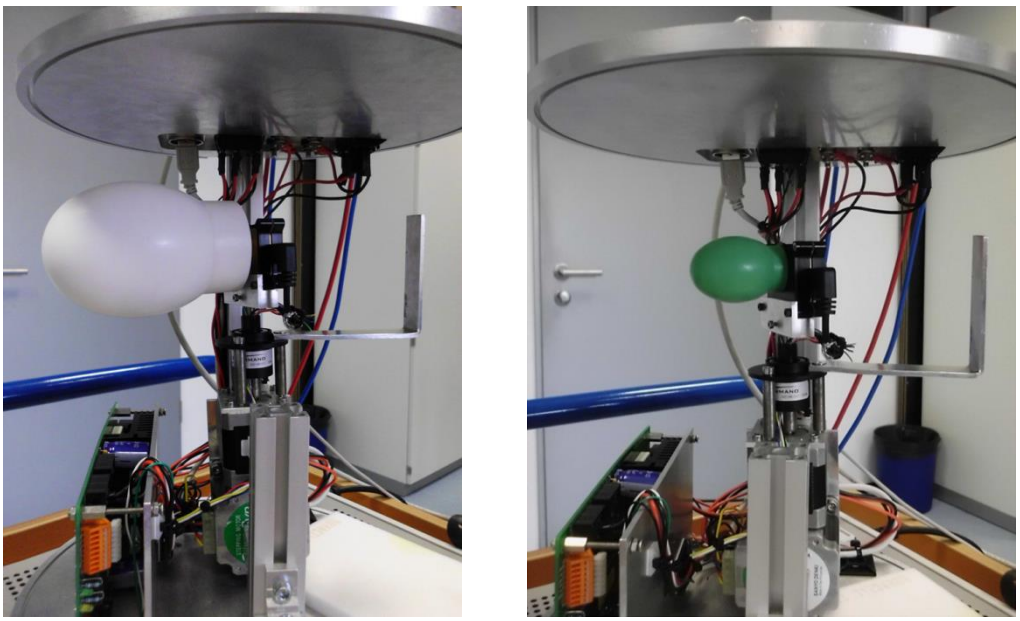

Fig. 3.21: MPR with large antenna (left) and small antenna (right)

Fig. 3.20 shows the result of a one-dimensional scan in azimuth from -45° to 45° while the elevation angle was fixed to 90°. For this measurement a radar bandwidth of 25 GHz was used, which results in a range resolution of about 6 millimeters. The received signal was multiplied with a hamming shaped window in time domain to suppress side lobes in frequency domain. On the left the image generated with the smaller antenna aperture is shown. The most obvious target is the trihedral reflector at 2.7 m distance (cp. Fig. 3.18). Taking this as a reference, the dynamic range of the image is as high as 80 dB. Some spread of the reflector in range can be observed, but its amplitude is 50 dB below the maximum reflection.

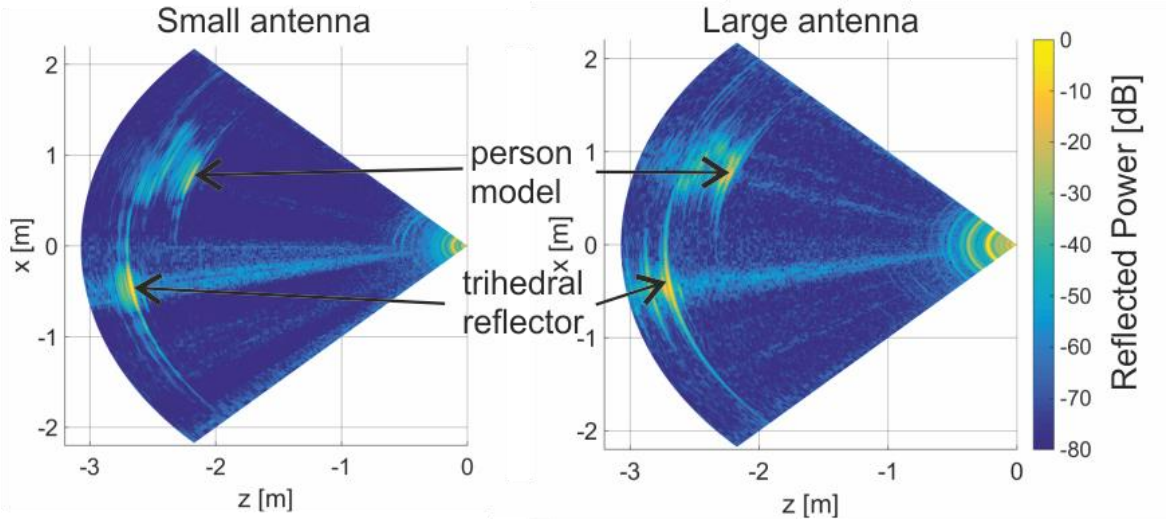

Fig. 3.20: 2D image of characterized scene with small and big antenna aperture

The spread in azimuth is due to the finite beamwidth of the generated antenna pattern. The second target within the image is the person model whose reflection can be seen in the upper half of the radar image. The front of the model leads to a strong reflection. Due to the fraction of the radar signal which is transmitted through the model's material, causing reflections on the backside, and its more complex shape the

reflection is more spread over the image plane. Nevertheless, the reflection by the front and smaller reflections by the arms at a slightly further range can be distinguished.

At the rightmost side of the images, the reflections of the dielectric lens can be observed. The strong reflections on the antenna surface even lead to multiple reflections within the antenna structure so that a range of about 30 cm is covered by the impulse response of the MPR. This impulse response does of course also lead to a spread of the measured targets. This gets most obvious looking at the reflection of the trihedral reflector. In Fig. 3.20, following the first reflection, a second peak can be observed 30 dB weaker than the main reflection at a range offset of about 5cm. Since this effect should be the same for all targets and stable over time, the issue could possibly be resolved by using a suitable calibration. The image on the right shows the measurement performed with the large antenna. The larger antenna size is evident from the strong reflection at small distances of about 15 cm. The blind range caused by internal reflections expands to about 50 cm. Also the spread of the two targets is higher as compared to the smaller aperture. Slightly more details from the person model get visible on the 2D plot generated from the larger antenna measurement data. However, maintaining the correct elevation angle has proven to be difficult when using a heavier antenna element. Especially for such high directivity a small misalignment already leads to significant increase of the free space path loss leading to a reduced dynamic range of the image shown in Fig. 3.20 on the right. To see the effect of the aperture size on the antenna directivity, the power reflected from the trihedral reflector is shown in Fig. 3.22 as a function of azimuth angle.

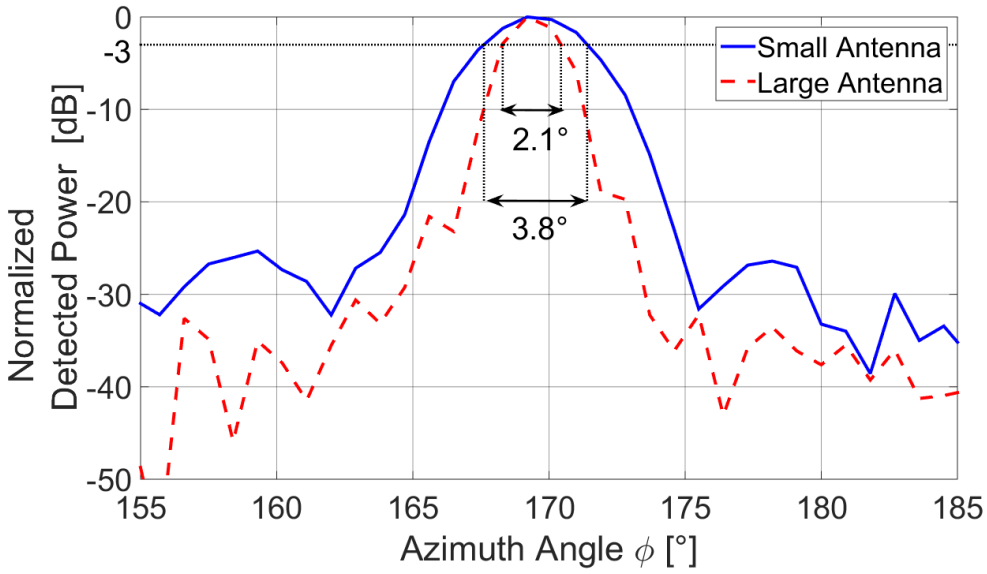

Fig. 3.22: Comparison of measured single target reflection as function of azimuth angle

The small antenna results in a 3dB spread of the single reflection of 3.8° in azimuth. The closest sidelobes can be found 10° from the main reflection 25dB below the main lobe. Increasing the antenna size clearly reduces the beam width. It is almost reduced by 50% down to 2.1°. Since the antenna is electrically larger as its smaller counterpart the sidelobes get closer to the main beam so that the closest ones are only

3° apart from the main lobe. At the same time the sidelobe suppression is reduced to 20 dB.

As described theoretically in section 2.5.1 it is evident from the experimental verification that increasing the antenna size improves the resolution of the generated image. On the other hand a large antenna structure leads to significant mechanical challenges enforcing a more stable mechanical design. Due to the specifications defined for the size of the MPR the smaller antenna will be used for the final prototype. Also with an angular resolution of 3.8° the quality of the generated data is expected to fulfill the requirements for a preliminary imaging system at this early stage of the project.

3.6.2. Comparison of different RF Sweep Bandwidths

While the angular resolution of the generated images is given by the aperture size of the used antenna, the range resolution depends on the bandwidth of the used radar signal. The FMCW module allows using arbitrary chirp bandwidths up to 25 GHz, thus the effect of choosing different bandwidths was experimentally investigated and is illustrated by the plot shown in Fig. 3.23. Here the power of the reflection caused by the trihedral reflector is shown as a function of range while the azimuth angle was fixed to -10°. For all three bandwidths, 5 GHz, 15 GHz and 25 GHz, the same chirp length of 4 milliseconds was used.

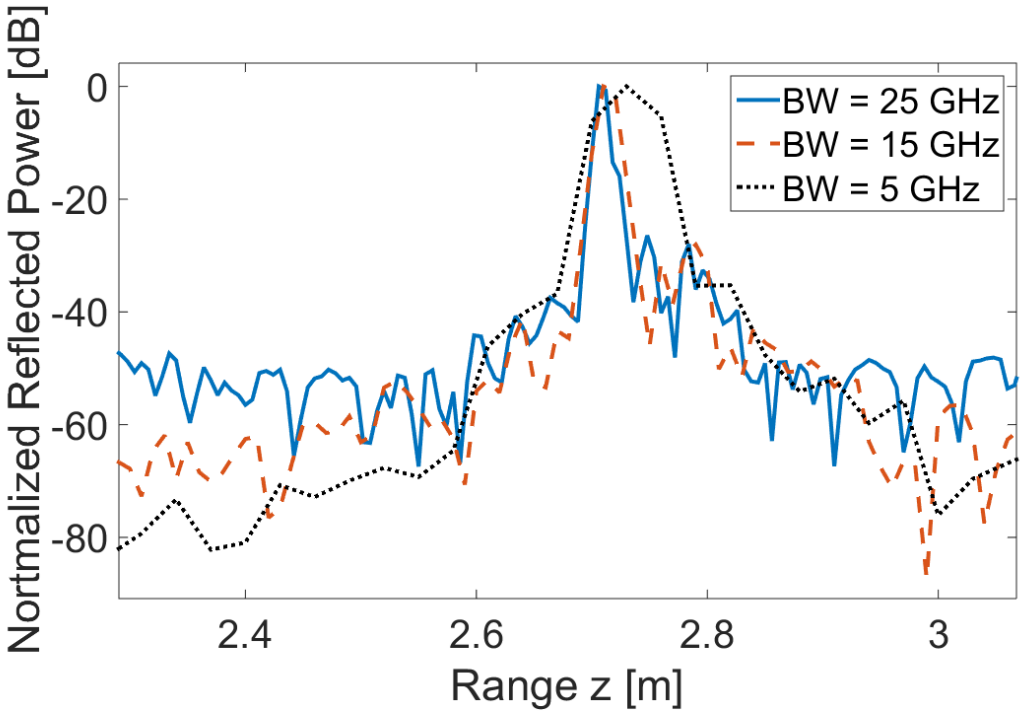

Fig. 3.23: Comparison of single target reflection for different radar bandwidths

Two effects can be observed. First the range resolution increases with increasing bandwidth. While 5 GHz chirp bandwidth leads to a 3dB width of a single reflection of 3 cm, increasing the bandwidth by a factor of 5 leads to a reduction of the 3dB width to 6 mm. Sidelobes are effectively suppressed using a hanning window in time domain. On the other hand reducing the bandwidth also reduces the power of the captured clutter and thermal noise. In Fig. 3.23 the dynamic range of the 5 GHz measurement

outperforms the 25 GHz measurement by 15 dB. Additionally a larger chirp bandwidth also increases the effect of the radars frequency response which is described in section 2.4.1. For broadband ranging effects caused by ripples in the characteristics of the module are increasingly affecting the image quality. A closer look on the measured profiles shown in Fig. 3.23 reveals that the high resolution measurement includes several sidepeaks within a distance of 10 cm above the main reflection. This is likely to be caused by the modulation of the signal amplitude while performing the frequency chirp. The low resolution profile measured with 5 GHz bandwidth does hardly show this effect. Therefore, effective calibration is crucial for high chirp bandwidths.

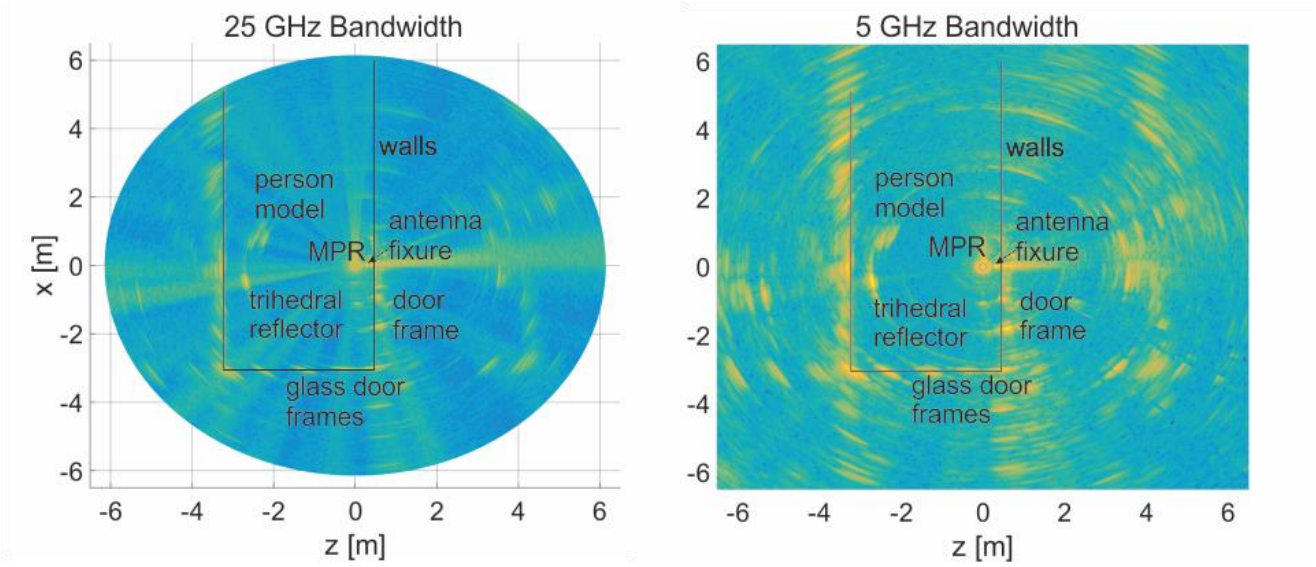

Fig. 3.24: 360° image in indoor environment using a bandwidth of 25GHz (left) and 5 GHz (right)

As stated in the DoW the MPR's purpose is to provide two dimensional information 360° around the robotic platform. Fig. 3.24 compares two 360° scans measured with full bandwidth (25 GHz) and 5 GHz radar bandwidth. The geometrical structures visible in the images correspond very well to the geometric arrangement shown in Fig. 3.24. The MPR itself can clearly be observed by the circular structure in the center of the image formed by the reflection at dielectric antenna's surface. Very close to this, on the right, a strong reflection can be seen. This is the mechanical fixture of the MPR at the surrounding of the MPR formed by a metal strip as visible in Fig. 3.21. It forms a clear marker for the azimuth angle reference. The surrounding walls can also be clearly identified. Especially corners formed by door frames lead to clearly visible reflections as obvious on the lower right and from the door at the bottom. Due to the limitation in intermediate frequency bandwidth (cp. Fig. 2.9) a change of sweep bandwidth changes the maximum range of operation (section 2.2). While for the 25 GHz image the range is restricted 6 m, 5 GHz would theoretically allow up to 30 m to be acquired with the available intermediate frequency bandwidth. Expending the maximum range for full resolution would require the expansion of the measurement time from the currently used 4 ms to a higher value. Also in this image the lowering of the bandwidth clearly increases the dynamic range of the measurement. Especially the wall on the left of the image shows off at a far higher contrast as compared to the 25

GHz measurement. In both images further targets can be observed behind the walls where they can hardly be caused by real reflections. This is caused by multiple reflections within the room. It is clear that the finally provided data has to exclude those virtual targets by suitable processing such as time domain gating and by the selection of the first or the strongest scatterer as described in section 3.7.

From an application point of view, a trade-off has to be made between high dynamic range and high range resolution. To combine both, higher measurement times would have to be accepted leading to a smaller image frame rate. Depending on the current use of the radar the parameters can be defined in order to match the requirements of the application scenario.

3.7. Data Processing Algorithms

Due to the purpose of the MPR as a laser-scanner-like operating device, some amount data processing is necessary in order to reduce the range profile data acquired by the FMCW radar sensor to multiple angle-range tuples. In the following sections, further explanation of the data processing is provided.

The information obtained by the radar module provides a reflectivity profile over distance for each azimuth angle. By this a 2D reflectivity image is formed. However, the sensor suite only uses a single distance and reflectivity value per angular step. Therefore each measured reflectivity profile has to be reduced to a single pair of range and reflectivity. For the MPR two methods are implemented, namely the nearest and the strongest scatterer. The same test scenario was used as already shown for other performance demonstrations.

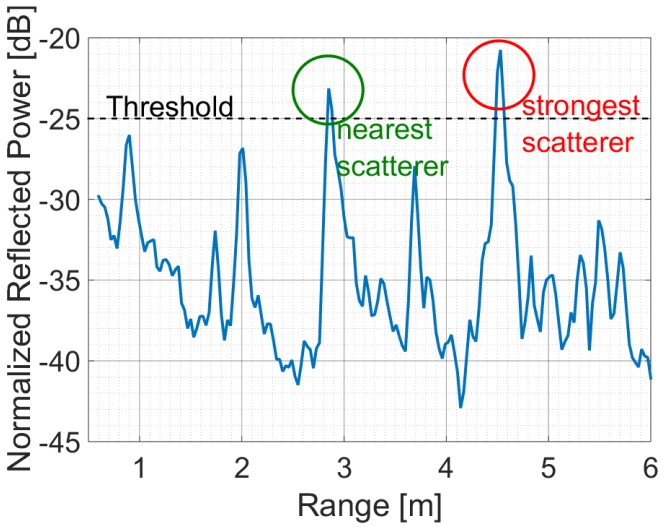

Fig. 3.25: Measured Reflectivity over range profile showing several reflections

Fig. 3.25 illustrates the identification of a data point from a single range profile. Several peaks can be identified. The most straightforward method is to detect the highest or strongest peak in the profile as marked by a red circle in Fig. 3.25. The entire profile is in this case reduced to a single data point (4.53 m, -20.75 dB). This method seems to be well suited for outdoor applications as well as to characterize the

dimensions of the room dimensions indoors since maximum reflection is typically caused by strong reflecting targets such as surrounding walls. However for controlling a vehicle the closest obstacles might be of higher interest. Therefore, the detection of the nearest scatterer has been implemented as an alternative method.

It is marked in Fig. 3.25 by a green circle. In this case the detection is slightly more complicated. To suppress peaks caused by clutter or noise a threshold has to be defined. In this case a normalized reflection of -25 dB was chosen. At this amplitude level only two peaks are present within the analyzed range window. The closer one is present at 2.85 m with an amplitude of -23.1 dB. If "nearest scatterer" is chosen this is the data point generated for the dataset which is transferred to the sensor suite. Fig. 3.26 shows the result of both methods if applied to a 2D radar image. The strongest scatterers are marked by red crosses while the closest scatterers are shown by white crosses on the right image. As discussed before the wall's reflections form the dominating strong scatterers.

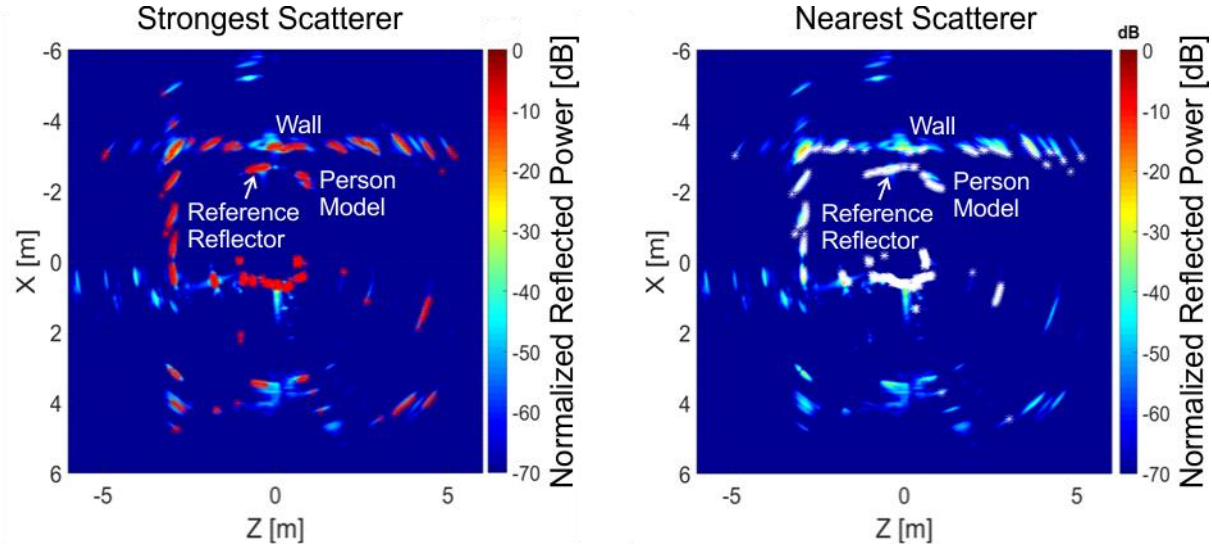

Fig. 3.26: Comparison of results obtained by strongest scatterer and nearest scatterer approach

The reference reflector and the polymer model appear relatively small since the outer part of their reflection falls below the amplitude of the reflection caused by the room wall. On the right the reference reflector and the person model appear far more prominent. They are close in front of the radar and form the nearest reflection. As a consequence of the applied peak detection, the ranges detected for each angle form a track around the radar acting as a "time-of-flight" distance detection. This is the basis for fusion with the data obtained from the laser scanning system. If the nearest reflection is used the obtained data sets should be quite similar. However, the threshold of the system has to be chosen carefully not to lose targets on one hand but also not getting distracted by clutter on the other.

The detection of the strongest scatterer is more reliable but might differ from the optically obtained data, especially if objects are detected which are partly transparent to the radar emission or do not completely cover the radar beam at any angle. The correct choice therefore mainly depends on the fact if the MPR is intended to be used as redundant system to enhance the reliability of the time-of-flight

measurement or if the results should complement the optical measurements characterizing the background in addition to the close targets being detected by the laser beam.

Having a closer look on the 1D profile shown in Fig. 3.25 leads to the observation that significantly more than 2 peaks have been detected. The lower 2 peaks have currently been filtered by using a threshold in amplitude. Especially close to the MPR this method might fail. As it can be observed on the reflection profile the noise level raises significantly towards lower frequencies. In conjunction with the reflection peaks caused by the surface of the dielectric lens in front of the MPR's RF port reflections high signal amplitudes would dominate the image especially if the nearest scatterer is detected. Therefore, range gating is implemented for excluding targets in the direct vicinity of the MPR from the post-processing.

3.8. ROS Interface Description

In the SmokeBot project, the Robot Operating System (ROS) is being used as a versatile development platform that allows an easy integration of the developed SmokeBot hardware and software components from the different project partners. Since it is used by a lot of developers in different fields all around the world, many robot related problems are already solved or can be solved with minimal adaption of already existing ROS packages. This makes ROS a very suitable choice for the scope of the SmokeBot project. As shown on the project website, the developers describe ROS as follows:

"ROS is a flexible framework for writing software. It is a collection of tools, libraries and conventions that aim to simplify the task of creating complex and robust robot behavior across a wide variety of robotic platforms."[13]

In the following sections the ROS interface development for the MPR is outlined and a detailed description of the used data structures is shown, to allow the project partners the extraction and processing of the measurement data gathered by the MPR.

3.8.1. Introduction

Beside the most current release, ROS is available in another release version, namely the "Long Term Service" (LTS) Release. Although both versions are actual stable releases, the software support for the LTS release is planned for a prolonged period of time (typ. 5 years after release) compared to the standard release and is thus recommended by the developers for applications that require a high degree of software stability over time.

To avoid any future compatibility issues that may arise, the LTS release was defined to be the development platform for the duration of the project and has thus been used in the development of the ROS MPR interface. As an underlying operation system the Linux distribution "Ubuntu 14.04 LTS" has been used as it is recommended by the ROS developers.

[13] http://ros.org

In order to give a more detailed description of the ROS interface development, a brief overview of the concept of ROS is shown. Basically, ROS offers a network infrastructure to allow a coordinated flow of data from different software applications running on the operating system as outlined in Fig. 3.27.

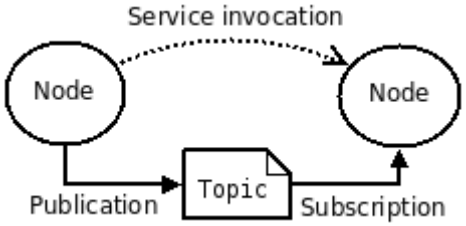

Fig. 3.27: ROS data flow (from ROS website)

These applications register with the ROS master as so-called "Nodes" that are able to either publish certain information or to subscribe to specific data channels of other nodes. In ROS terminology these data channels are called "Topics" and are used to structure the data flow within the entire Robot Operating System. To allow the data flow within each of these topics, the information needs to be encapsulated in so-called "Messages" that are exchanged with other nodes. It is noteworthy, that no information flows directly between the registered nodes, but instead, the ROS master is responsible for the reception and distribution of messages according to the subscription status of the nodes.

Messages that are being broadcasted by publishing nodes are of a specific message type. The message type is defined at compile-time and hardcoded into the node. Beside the builtin ROS message types, such as a laser-scanner message for example, ROS supports the usage of custom message types when necessary. In the context of the SmokeBot project, the MPR data will later be fused with the data from a laser scanner that is mounted on the same rotational axis as the MPR. Therefore efforts have been made to make the MPR measurement data look similar to data being published by a laser scanner node. This has been achieved by using an algorithm to reduce the target profile acquired by the MPR to a dataset that includes angle-range tuples. Thus there was no need to use custom messages so far, instead the predefined ROS **LaserScan** message has been used to encapsulate the MPR data. After startup of the MPR ROS node, a new topic named **mpr_scan** is registered with the ROS master that contains the LaserScan messages emitted by the MPR ROS node.

3.8.2. Node description

The development of the ROS node has been carried out using C++ and the Gnu Compiler Collection (GCC) on Ubuntu Linux. Beside the registration as a publishing node and the actual publishing of the data, the application is responsible for configuring the FMCW radar module and setting up the rotary movement. Also the repeated starting of new measurements and the collection and processing of the radar data is being done by the MPR ROS node.

Once the application is started, the MPR constantly runs measurements so that a permanently updated message stream is available without further external input to the MPR. As stated before, the data produced by the MPR node is available as ROS **LaserScan** messages within the topic named **mpr_scan** as further described in the next section.

3.8.3. Parameters and Data Structures

Measurement data being published by the MPR ROS node is encapsulated in a standard ROS LaserScan message. Although this message type is intended to be used with Rotary Laser Scanners, it has deliberately been used to implement the MPR interface to make it look like a Laser Scanner as much as possible. This allows other project partners to apply Laser Scanner processing algorithms to MPR data without the need to change the algorithm interface. In the context of the SmokeBot project, a sensor fusion between a Laser Scanner and the MPR is planned as a work package, thus it is mandatory that the interface of both hardware units look similar.

Parameter name	Description	Value (MPR)
Float32 angle_min	Start angle of the scan [rad]	0
Float32 angle_max	End angle of the scan [rad]	2π
Float32 angle_increment	Angular distance between measurements [rad]	1.8°
Float32 time_increment	Time between measurements [seconds]	2 ms
Float32 scan_time	Time between scans [seconds]	0.4 ms
Float32 range_min	Minimum range value [m]	0.1 m
Float32 range_max	Maximum range value [m]	50 m
Float32 [] ranges	Range data [m]	
Float32 [] intensities	Intensity data [device-specific units]	

Table 3.3: ROS LaserScan message in MPR context

The radar sensor used in the MPR performs a 360° turn with an angular frequency of 2.5 Hz. Therefore the angles reported in the message are defined to be 0 and 2π for **angle_min** and **angle_max** respectively. During a single revolution, the MPR acquires 200 measurements, thus the value reported for **angle_increment** is set to 1.8°. Correspondingly the **time_increment** parameter is reported as 2 milliseconds to achieve the 2.5 Hz scan rate and **scan_time** is reported as 0.4 milliseconds. The parameters **range_min** and **range_max** define the minimum and maximum scan range and are determined by the radar configuration and the minimum range gating distance. They are reported as 0.1 meters and 50 meters respectively.

Due to the basic working principle of radar sensors, each performed measurement delivers a range profile containing multiple targets that have been acquired by the radar sensor. The information in the range profile is then reduced by using different techniques outlined in section 3.7 to obtain a single distance and intensity value per each azimuth angle. This information is then published through ROS using the vectorized parameters **ranges** and **intensities**.

The MPR node software package is also used to control the pivoting movement of the radar sensor. For this purpose, a controller board is used within the electrical

setup of the MPR, which is connected using a RS232 interface. However, further information, as in motor position or motor speed is not being published through ROS.

Using the developed ROS node software implementation, the MPR can be embedded in the overall structure of the robotic platform that is used in the SmokeBot project. Therefore it can be used as a part of a complex remote measurement system for exploring the surroundings of the SmokeBot, even in situations when the laser scanner provides only poor quality data, such as smoke or dust in the air.

We want to emphasize that the ROS software implementation provided and described at this point in time should be considered as fully functional and sufficient to perform basic measurements. However we are planning to introduce software enhancements that may arise due to feedback from the project partners in the future, thereby enabling the project partners to achieve the goals set in their work packages.

Additional information for the practical implementation of the developed 2D MPR system regarding the ROS node software is available as a Quick Start Guide in the appendix 8.1.

4. 3D Mechanical Pivoting Radar

As described earlier the MPR is not necessarily restricted to 2D imaging. If the mechanical design allows steering of the antenna element in azimuth and elevation 3D images can also be generated. For static objects this approach can generate far-field images with the same resolution as a fully populated MIMO array of the same aperture size. Due to technical restrictions the final MIMO will not be completely filled. In other words, the number of array elements needed for an equidistant array spaced by half a wavelength over the entire aperture, cannot be realized with justifiable technical effort. This does not necessarily restrict the resolution of the generated image. Rather, the geometrical distribution of the antennas can be optimized for maximum resolution or dynamic range, depending on sidelobe suppression. The imaging performance of an antenna array is commonly described by the point spread function of the array. It expresses the spread of a single point target over the image. In the far-field the generated image can be described as the perfectly resolved radar image convolved with this function. Therefore the expected image can be predicted for each MIMO configuration if an image with significantly higher resolution as the array's point spread function is available. The MPR measurements in three dimensions therefore allow the generation of first static images.

The following section will describe the mechanical structure of the 3D antenna steering and the electrical implementation. Since the antenna has to be turned in azimuth and elevation two stepper motors are required. The mechanical approach is briefly described to allow a deeper understanding of possible operation modes and their mechanical limits. Based on this the specifications of the 3D MPR are listed and discussed. Finally projections of generated 3D images are shown to visualize the performance of this first radar system and provide a first impression of the final imaging results expected to be available in real-time at the final stage of the SmokeBot project.

4.1. Mechanical and Electrical Setup

For the 3D MPR most of the fundamental modules of the 2D MPR can be adopted. The motor controller has been previously selected on the assumption that the control of a second motor is provided, although the 2D MPR only requires movement in a single axis. In contrast, the 3D MPR is capable to turn the radar additionally in the elevation direction, demanding a second motor as shown in Fig. 4.1.

As the motor controller board supports a wide a range of different stepper motors, it has been possible to choose suitable motors for azimuth and elevation, which differ in their requirements. Apart from the additional motor, no further hardware changes had to be implemented in comparison to the 2D MPR. Therefore no modifications in the electrical interface have been made and the wiring is very similar.

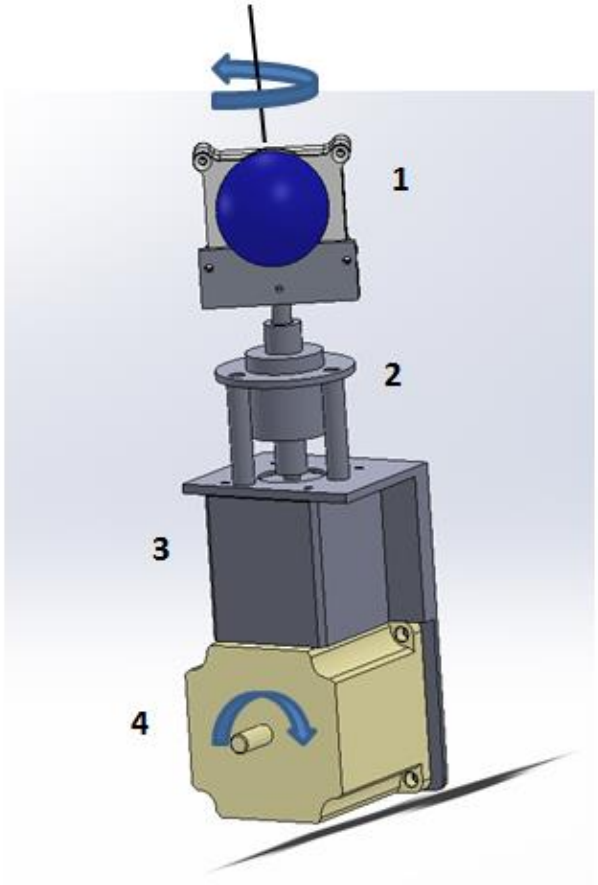

1 – FMCW Radar Module
2 – Slip Ring
3 – Azimuth Motor
4 – Elevation Motor

Fig. 4.1: CAD drawing of 3D mechanical beam steering concept

The basic functionality of the radar's azimuthal movement has been derived from the 2D MPR, thus the azimuthal beam steering control can be reused and the design of the assembly (slip ring, mechanical radar mount and shaft extension) does not need to be modified.

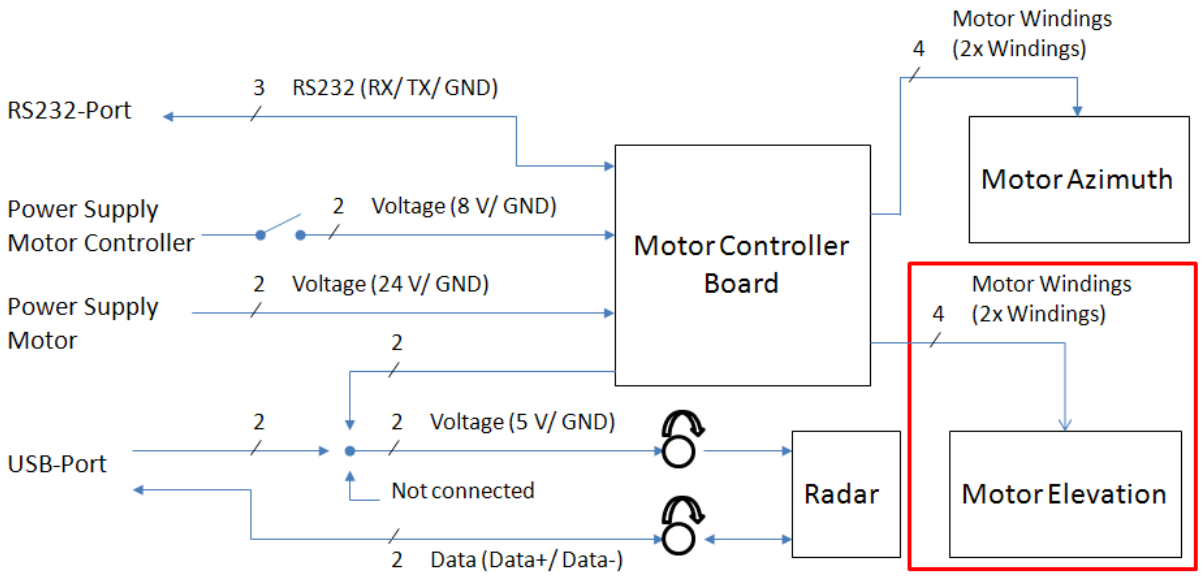

Fig. 4.2: Circuit and Signal Flow for 3D MPR

However, considering the requirements for the azimuthal motor, a different motor type has been selected. This is due to the fact, that the axis of rotation is not always collinear to the gravity vector, because the angle of elevation can change. Therefore the motor is presented with an extra load resulting in additional torque, which has to be considered.

The momentary force caused by the extra load reaches its peak value, when the gravitational vector is perpendicular to the axis of rotation. Correspondingly, this is the point, where maximal motor torque is required[14]. In respect to this worst case, the motor has to be selected. For the azimuth rotation of the 3D MPR the same parameters apply as for the 2D MPR in regard to maximum speed and acceleration. As seen in section 3.2.3, the motor torque for rotating the radar is relatively small. Therefore it is neglected in the following consideration. Instead the motor holding torque is estimated for the case when motor is stopped under worst case conditions (see Fig. 4.3 right).

The torque τ in this case is simply calculated with the following equitation, whereas r the distance of a weight force F to the axis of rotation is.

$$\tau = r * F$$

For a first rough assessment, the two point mass model from section 3.2.3 is reused. The weight of radar module inclusive antenna flange and the antenna itself are about 70 gramm and 75 gramm respectively. The corresponding weight forces are about F_{radar} = 0.7 N and $F_{antenna}$ = 0.75 N.

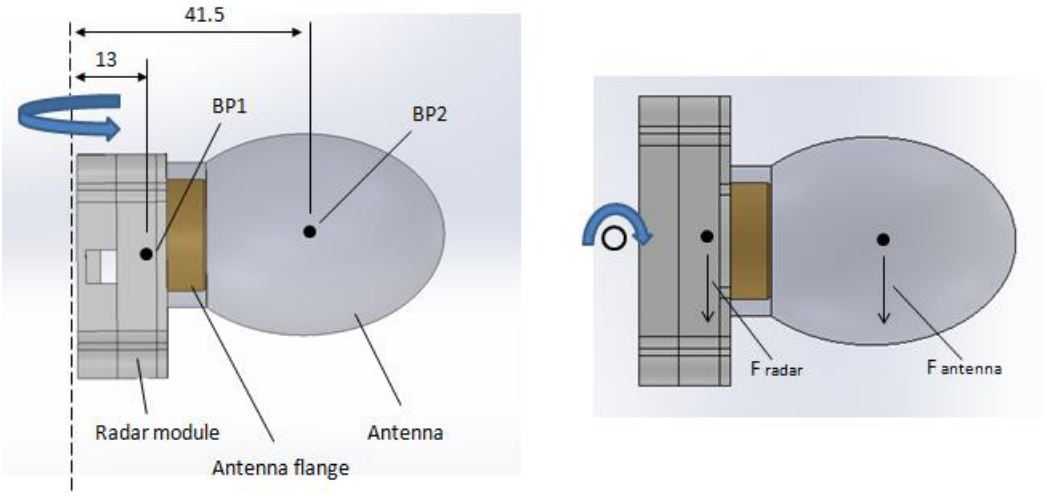

Fig. 4.3: Balance points of radar (left) and antenna (right) for worst case horizontal rotation

Using the distances from Fig. 4.3 (left), a minimal holding torque of 4 Ncm is calculated.

$$\tau_{holding} = F_{radar} * 0.013\,m + F_{antenna} * 0.0415\,m \approx 40\,mNm = 4\,Ncm$$

[14] This point is reached, when elevation angle is 90° and the radar is oriented horizontally.

In order to allow for some headroom, for the required acceleration torque that has been neglected in the calculation, a stepper motor (see Fig. 4.4) with a holding torque of 31 Ncm was selected. The reserves are also important, when taking in account, that motor torque is reduced with rising speed. In normal operation of the 3D MPR the motor current is set to 300 mA. Comparable to the Azimuth motor from the 2D MPR, the chosen motor features a 1.8° basic full-step angle, which is halved to 0.9° in half step mode.

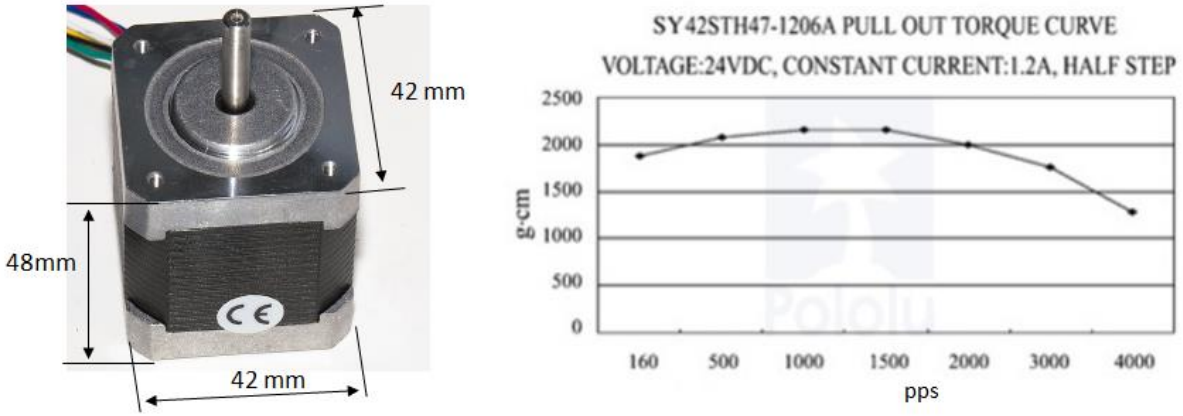

Fig. 4.4: Azimuthal axis stepper motor dimensions and torque characteristics

In order to select a suitable motor for the elevation axis, a simple model for determining the minimal holding torque (similar to the one of the azimuthal motor) was created. Based on the chosen azimuthal motor above, the different components were grouped to three point masses. Their locations in regard to the assumed elevation axis were defined by the balance point of the respective group. In Table 3.3, these groups are listed. The weight forces resulting from their masses and the distances to the rotation axis are also shown.

Group	Balance Point	Components	Total weight	Weight force	Distance to rotation axis
1	BP1	Motor for azimuth rotation	350 g	3.5 N	24 mm
2	BP2	Distance bolts Shaft extension Slip ring	75 g	0.75 N	74 mm
3	BP3	Radar Module Antenna flange Antenna Mechanical radar mount	165 g	1.65 N	107 mm

Table 4.1: Component groups of the azimuth rotation assembly

In Fig. 4.5: Balance points of the respective groups of the elevation rotational model overview about the model for the elevation axis are shown.

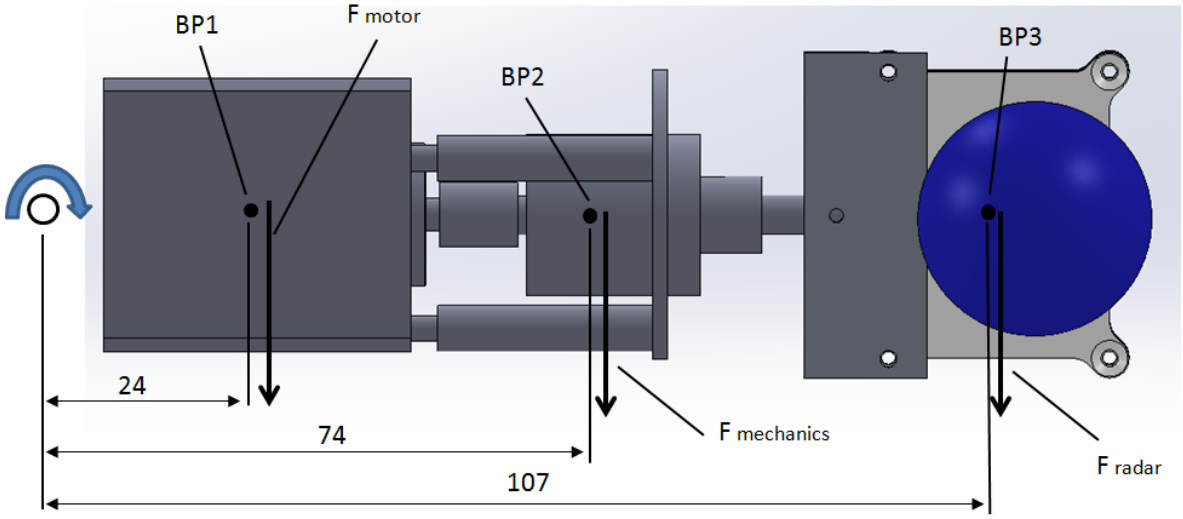

Fig. 4.5: Balance points of the respective groups of the elevation rotational model

With the data from Table 4.1, the minimal holding torque for the elevation motor is estimated.

$$\tau_{holding} = F_{motor} * 0.024\,m + F_{mechanics} * 0.074\,m + F_{radar} * 0.107\,m \approx 31.6\,Ncm$$

As before, attention was taken to ensure a certain amount of headroom when selecting a suitable motor due to the rough estimation of weight forces. Additionally, for this application a motor with a double-shaft has been chosen. This allowed an implementation with only minimal bending moment applied to the shaft, thus stabilizing the measurements.

In consequence a stepper motor with a holding torque of up to 85 Ncm was choosen (103-H7123-5010). Its outline dimensions and torque/speed curve is shown in

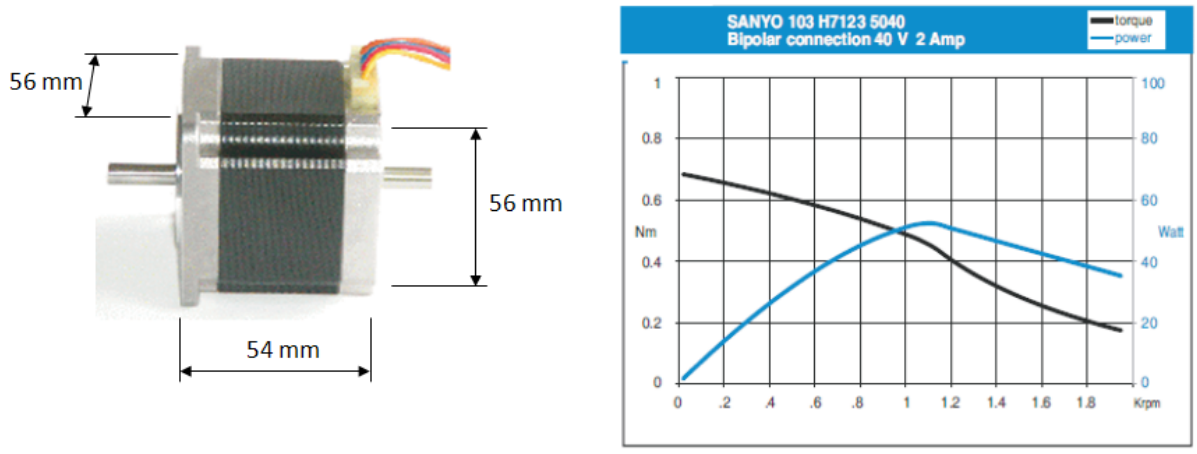

Fig. 4.6: Elevational stepper motor dimensions and torque characteristics

Fig. 4.6. It should be noted, that the maximum available motor power cannot be used, due to supply voltage limitations on the motor controller board. However, since the elevation axis will be driven in stepped measurement mode only, no high constant motor speeds are required in this application. Additionally, enough torque headroom has been encountered for. Thus, this is only a minor limitation which does not restrict the 3D MPRs performance. The basic full-step angle of this motor is equal to the azimuthal motor. Therefore the elevation angle can be adjusted with a step size of 1.8° in full step mode and 0.9° in half step mode.

In the following figures the implementation of the 3D MPR is shown by means of CAD drawings.

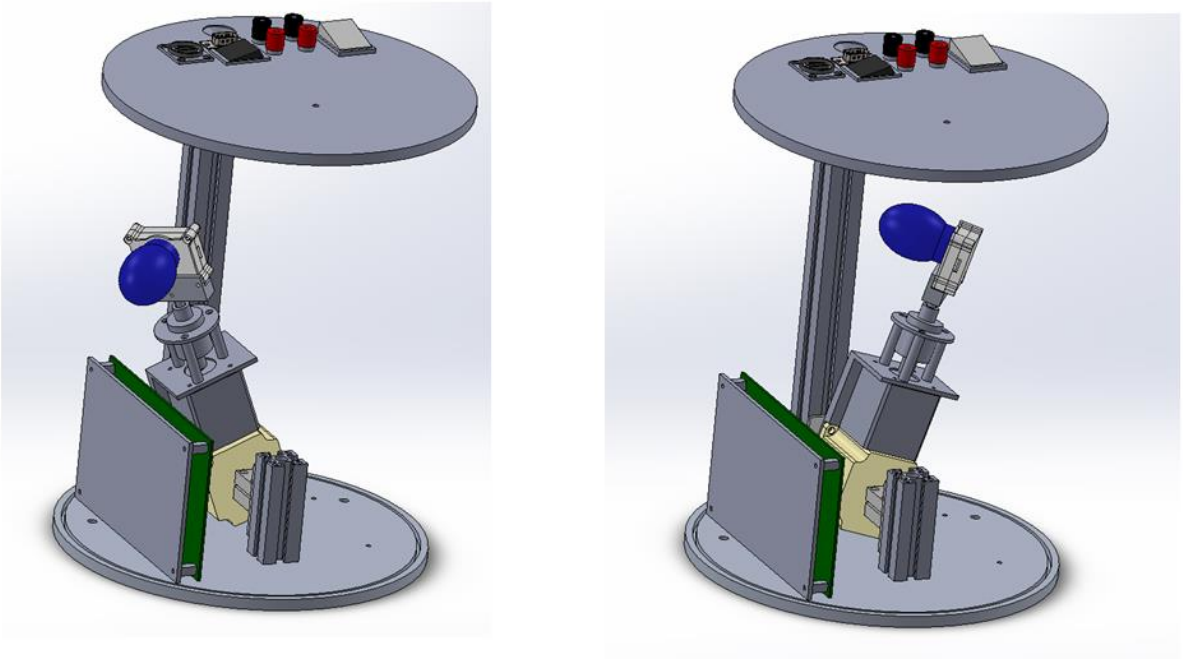

Fig. 4.7: 3D MPR CAD drawings

As for the 2D MPR, a reference target for data alignment is used. This is done by measuring the reference in every 360° turn. The possible angular range for elevation is limited with bumpers mounted on the ground plate (bottom). This is intended to secure the motor controller board and radome (when applied) from getting damaged by moving parts. However, due to the limitations by the top and bottom part of the case, an elevation range of -30° and + 15° can be used.

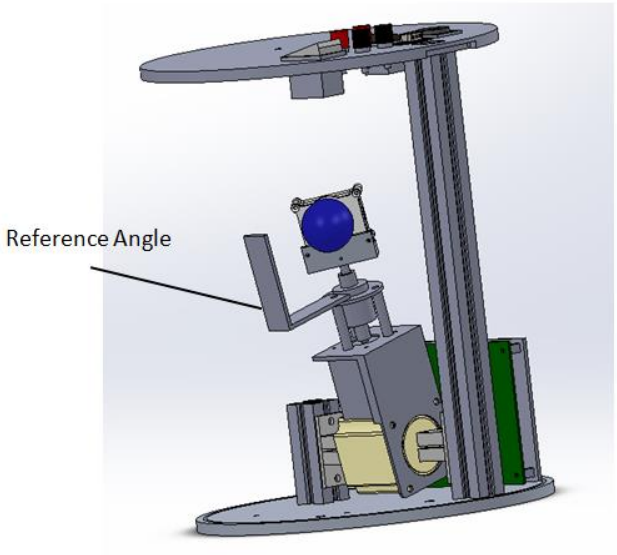

Finally Fig. 4.8 shows photographs of the fully integrated 3D MPR.

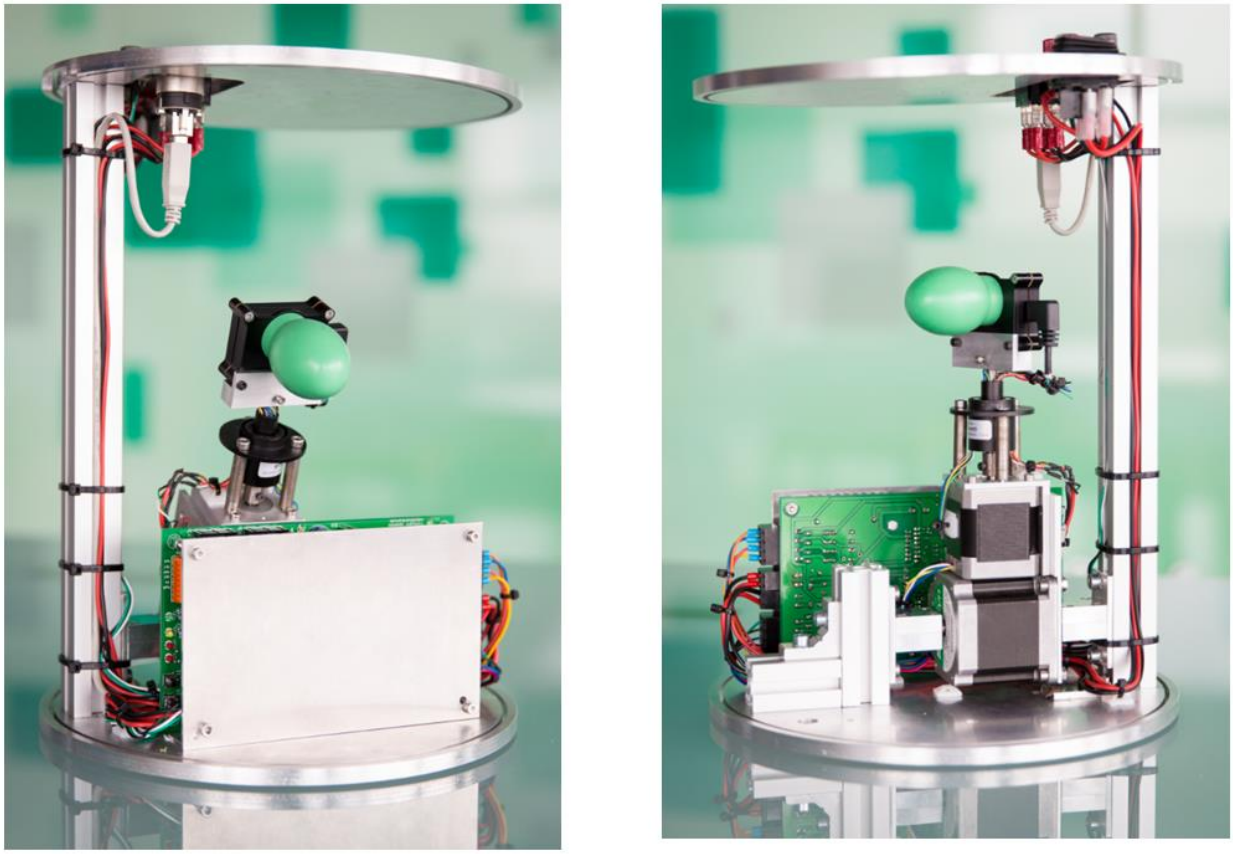

Fig. 4.8: Photograph of fully assembled 3D MPR

4.2. **Image Formation Algorithm**

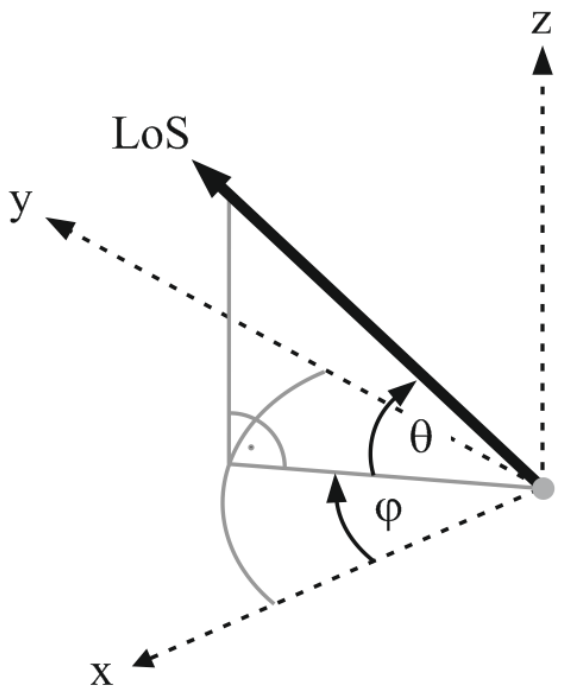

Fig. 4.9: Spherical Coordinate system used for MPR based image formation

In order to be able to generate 3D images, it is crucial to define the coordinate system where the measured data is mapped. The radar module used for the MPR only obtains range profiles as a function of distance *r*. The used antenna focuses the measurement only to detect targets which are within the narrow beam of the radar module. By mechanically turning the radar module this range profile is measured pointing at different angles.

For complete 3D images the MPR has to be moved in azimuth φ and elevation θ direction. The elevation is defined as the angle from the xz-projection of the vector pointing to the detected object. It therefore provides the height information which is mapped on the y-dimension in the chosen coordinate system. This is shown schematically in Fig. 4.9. For the 2D MPR used in this project the elevation angle θ is fixed to 0 degrees restricting the measurement to the xy-plane.

4.3. Imaging Example

To show the 3D imaging capabilities of the two axis version of the MPR as similar scenario as for the 2D images was used. A photograph of the arrangement is compared with the resulting image in Fig. 4.10.

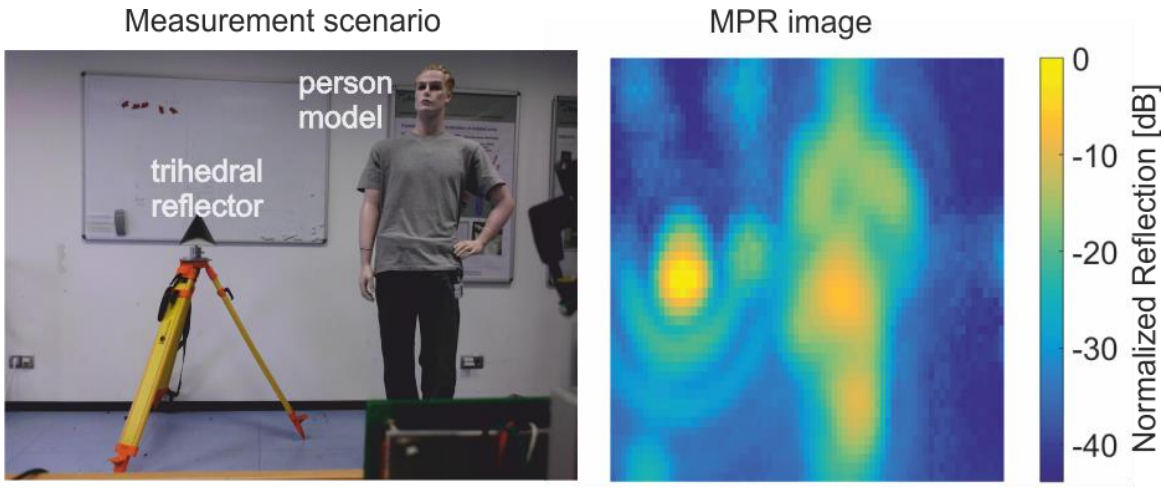

Fig. 4.10: Front projection of 3D image generated with 80 GHz MPR with 25 GHz bandwidth

The model of a standing person adds some 3D complexity to the image. A trihedral reflector was used to obtain information about the point spread function of the used radar in azimuth and elevation. During the imaging process the small antenna with 18 mm aperture was used moved in 0.9° steps in both axes. The radar is operated in full resolution (25 GHz) mode with a chirp length of 4 milliseconds. Both, the trihedral reflector as well as the plastic model were placed about 3 meters in front of the MPR. To obtain a 2D projection of the measured 3D data the reflected power within a range block of 0.5 m around the targets has been numerically integrated. The result is shown in Fig. 4.10.

The generated image has a dynamic range of more than 40dB. As one can see on the left of the radar image the reference reflector leads to a very strong reflection surrounded by circular structures. These are due to the antenna sidelobes described in section 2.5.2. The sidelobes are also visible around the image caused by the person model where they show up in a corona like shape. The persons head, arms and legs can clearly be identified. While the right leg leads to a bright reflection, the left leg stands slightly behind so that it is significantly weaker on the image. The bright spot in the centre of the person is caused by a metal belt-buckle.

It can be seen that images of reasonable quality can be generated with the 3D version of the MPR. Since this is supposed to be used as basis for the prediction of later MIMO images the result shown in Fig. 4.10 can be seen as reference for an ideal MIMO array. The next step is to see the degradation due to the limited resolution and dynamic range which can be obtained by the MIMO array. These results are shown in the following sections.

4.4. Preliminary MIMO Performance estimation

The aim of the radar module development within the SmokeBot project is to provide a MIMO based radar camera system, which enables full 3D imaging in real-time. As this module is only available in a later stage of the project the measurement capabilities of the MPR are used to give an outlook towards the results which can be expected by the final module. As discussed earlier the angular resolution of the radar is given by its aperture. Therefore, knowing the aperture of the designed MIMO array allows predicting the image quality of images generated by the final system. A first example of a designed MIMO array is shown in Fig. 4.11. The transmitters form the outer circle of the array while the receivers are placed concentrically from the center. The resulting virtual array can be interpreted as a phased array delivering the same performance. It is also circular with a quasi-random distribution with increasing density towards the center.

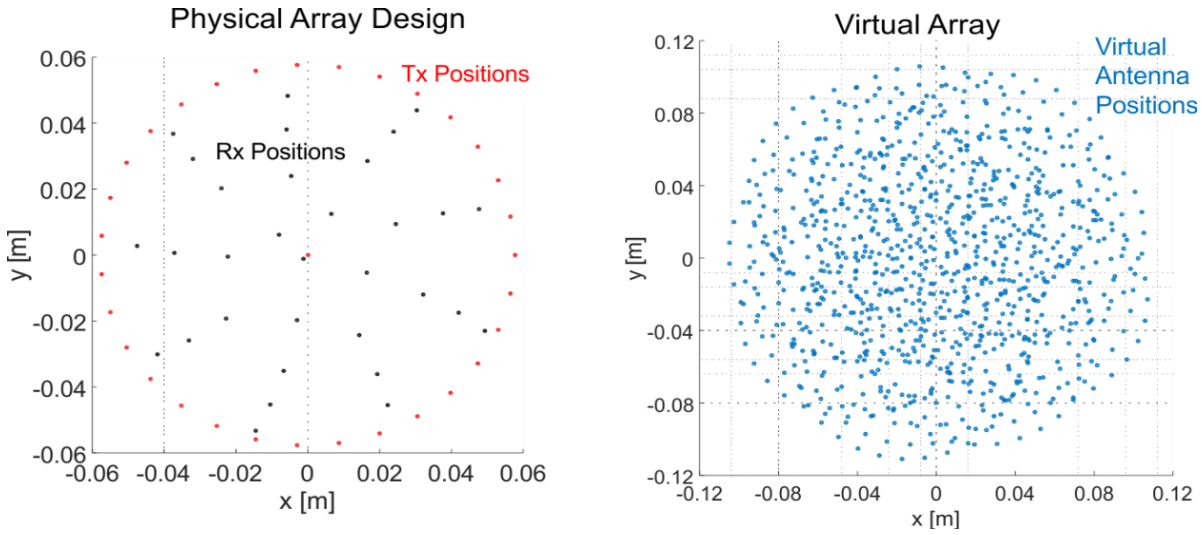

Fig. 4.11: Example of curvilinear MIMO array

The aperture size of the proposed virtual MIMO array leads to a highly focused beam. The Theoretical calculation results in a 3dB beamwidth of 0.7° in azimuth as shown in Fig. 4.12. This is encouraging as it would enable far better resolved images as compared to the current MPR. The main limitation arises from the sidelobes. Very close to the main beam two narrow sidelobes occur at 25 dB below the main lobe power. At +/-4.8° the strongest sidelobes are 23.7 dB below the main lobe. This clearly limits the dynamic range of the imaging system. It will be a key part of the further design work within the project to optimize the MIMO array design for an optimum trade-off between dynamic range and angular resolution.

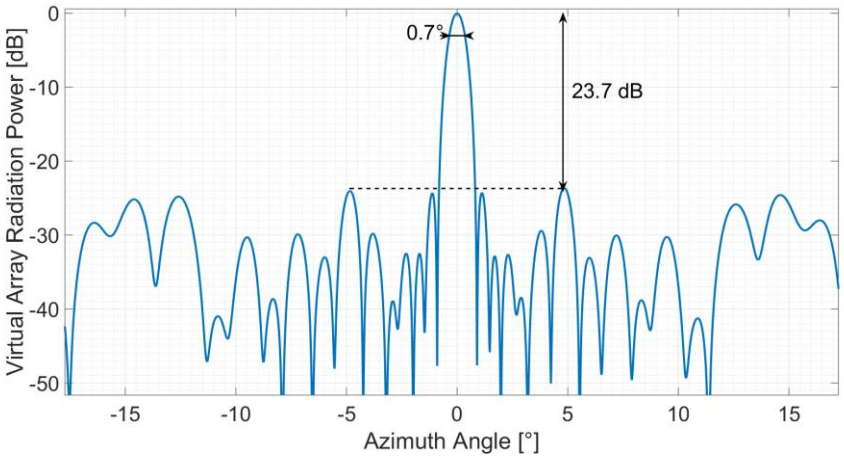

Fig. 4.12: Radiation pattern of MIMO array as a function of azimuth angle

The signals measured by MPR have a noise level of -25dB. The signals obtained by the convolution have a noise level of -22dB. This means that the noise level increases by 3dB due to the focusing pattern of the MIMO array. This situation can be seen in the radar images obtained by MPR and the convolution, in Fig. 4.13 and Fig. 4.14. The noise level slightly increases along all range directions.

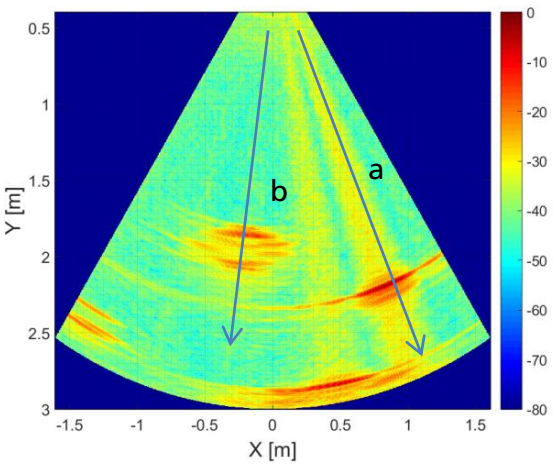

Fig. 4.13: 2D image with reference reflector (right) and person model (left) detected by the MPR

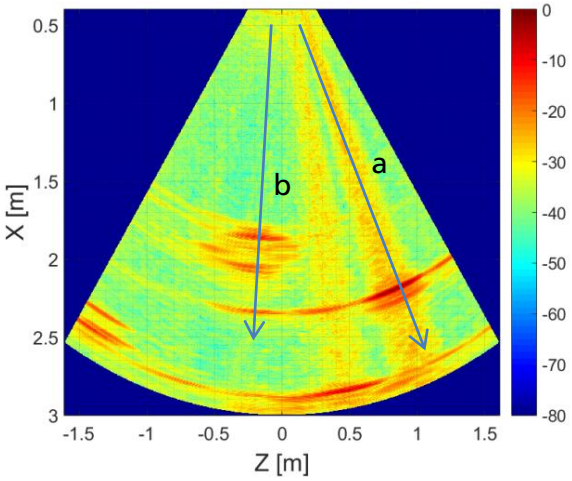

Fig. 4.14: MPR image convolved with MIMO radiation diagram for MIMO performance estimation

In Fig. 4.14, a potential image generated by the MIMO array is presented. Since the data obtained by the MPR was used, the resolution is restricted by the angular resolution of the raw data. However, the effect of the sidelobes can be clearly observed. The overall noise level is increased by 3dB due to mutual crosstalk of the noise within different angular bins at the same range. Especially the strong reflection from the reference corner reflector in look-angle a) leads to significant angular crosstalk. In look angle b) a virtual target appears behind the reflection caused by the person model. Although being critical for 2D image generation this sidelobe caused crosstalk might

not affect the generation of the “time-of-flight vector” provided to the sensor-suite. The crucial parameter for this will be the detection threshold. Therefore, the intended dynamic range is a key parameter for the MIMO array design. Significantly higher dynamic ranges can be obtained by enhancing the density of the virtual antenna elements. For a given number of transmitters and receivers, being restricted by hardware constraints, this automatically reduces the arrays cross section, thus reducing the angular resolution. The definition of this trade-off should be done in discussion with the potential users of the system to enable the array design to adopt to the requirements of the SmokeBot system.

5. Summary

In this document, the work regarding the MPR, carried out by Fraunhofer FHR in the WP1.1 from M1 to M10 has been described. Beginning with the motivation and intent behind the MPR based around save-and-rescue operations, the need for a radar system described in this document has been presented. The requirement of acquiring intelligence about emergency situations in unknown environment is a common scenario in today's daily life that nowadays is being approached by the use of 3D laser scanners. These scanners have their limitations when used in harsh environments. We have shown that it is technically feasible to support the laser scanner in its operation during foggy and cloudy environments by means of the mechanically pivoted radar. Thus, in scenarios with poor visibility, the unreliable information of the laser scanner could be sensor-fused with data from the MPR that is not depended on optical visibility.

Following the introduction, the basic working principle of radar systems in general, as well as the FMCW radar system being used in the MPR is illustrated. From the basic understand of linearly frequency modulated frequency sweeps, important theoretical relations to the data generated by the radar system are being derived and are accompanied by example figures. Subsequently the FMCW radar module that is being used within the MPR is introduced in detail. Important key features that are relevant to the information quality of the MPR are shown and discussed by disclosing the hardware architecture. In addition, further characterization of the radar module such as Output Power and IF Bandwidth have been carried out and shown on the basis of measurements.

An important detail for the suitability of the radar module to use in the MPR is the achieved beam width of the antenna that is being used. Therefore in section 2.5, a brief introduction to RF based geometric imaging and the impact of antenna beamwidth on imaging performance has been presented. This is followed by a detailed description of the used elliptical lens antenna and its basic working principle. The section concludes with the achieved radiation pattern and the achievable beamwidth as well as the actual antenna realization.

Beginning with section 3, the concept and design that stand behind the MPR are shown in detail along with the requirement it has to meet and the actual implementation that has been chosen. The section continues by explaining the basic mechanical and electrical setup as well as showing the design assumptions and calculations that have been made. In addition, the general electrical interface is shown and the available control parameters are listed to give an impression of the abilities of the fully integrated MPR. Also by means of photographs of the finished device, an impression of the finished MPR is given. The section continues by presenting information on how to use the electrical interfaces of the MPR and shows a summary of the MPR's electrical, mechanical and acquisition specifications. A summarized version of these sections can be found in the Appendix 8.1. Additionally, the image formation algorithm that is used to extract radar information from the MPR during its 360° scanning operation is shown. These algorithms have been verified using MATLAB and example results of MPR plots have been given. Following these demonstrations, further

experimental evaluations such as the comparison of different antenna aperture sizes and their impact on image quality have been carried out and are shown as well as the impact of using different RF sweep bandwidths. The section is further concluded by introducing algorithms that are used to reduce the information acquired by the radar sensor to angle-range tuples so that the data being delivered by the MPR can be easily fused with any laser scanner information at a later stage in the SmokeBot project. Algorithms such as "nearest scatterer" and "strongest scatterer" as well as the effect of thresholding and range gating are shown and explained by using real example measurements. To conclude the chapter, a section presenting the efforts on implementing a ROS node interface for the MPR has been included. Here, important parameters and definitions concerning the ROS node are shown and summarized to allow the project partners an easy access to the data provided by the MPR without having to implement a custom to-be-defined API.

In the following chapter 4, a step towards closing the loop to the planned MIMO radar camera has been done. By adding a second rotational axis to the 2D MPR, 3D image formation has been made possible. Accordingly the concept and design of the so-called 3D MPR have been presented along with its final realization. In the following section, a brief introduction to the 3D image formation algorithm is given and the MPR's 3D imaging capabilities are demonstrated by showing an imaging example of a complex scene in direct comparison to a photograph. To conclude the preliminary MIMO performance estimation, one of the candidates for the MIMO array topology that is to be realized in the Tasks 1.2 and 1.3 is shown, alongside its radiation and sidelobe performance. To finalize the estimation, the 3D MPR image has been convolved with the theoretical MIMO radiation diagram in order to preliminarily evaluate the MIMO imaging performance. The results are given in 2D sector images and the concluding performance estimation and trade-offs have then been discussed. The chapter has been concluded by highlighting the important differences and trade-offs between the MPR and the MIMO based radar camera along with its advantages and disadvantages. These results will be further used within the Tasks 1.2 and 1.3 for the development process of the Radar Camera (Task 1.2 and 1.3).

6. List of Figures

Fig. 2.1: Detection and Ranging using a pulsed radar system 7
Fig. 2.2: FMCW Radar System Architecture 8
Fig. 2.3: FMCW Radar System working principle 8
Fig. 2.4: Time domain and corresponding frequency/spatial domain representation 10
Fig. 2.5: Photograph of Radar Module in Case 11
Fig. 2.6: Photograph of frontend and backend of the radar module 11
Fig. 2.7: Radar Module Architecture 12
Fig. 2.8: Measured available transmit power of radar module 14
Fig. 2.9: IF Frequency response of the radar module 15
Fig. 2.10: Antenna as sum of omnidirectionally radiating elements 16
Fig. 2.11: Comparison of mechanical and phased array beam steering 17
Fig. 2.12: Geometrical Design of Elliptical Lens 18
Fig. 2.13: Dielectric Lens Antenna with cutplane 19
Fig. 2.14: Radiation diagram of small and large dielectric antenna as a function of azimuth angle 20
Fig. 2.15: Simulated radiation pattern of large and small aperture dielectric antenna 20
Fig. 2.16: Transient E-field simulation at different time steps. 21
Fig. 2.17: Realized antenna assembly 21
Fig. 3.1: CAD drawing of the mechanical beam steering concept 22
Fig. 3.2: CAD drawings of the 2D MPR 24
Fig. 3.3: Circuit and signal flow diagram of the 2D MPR 25
Fig. 3.4: Switch function of radar switch 25
Fig. 3.5: Photograph and CAD drawing (in mm) of the 80 GHz FMCW radar module 26
Fig. 3.6: FMCW radar mounted on stepper motor and slip ring 27
Fig. 3.7: Slip Ring RS-HX2512-002 and its specifications 28
Fig. 3.8: Balance points of radar module and antenna 28
Fig. 3.9: Outline dimensions and torque/speed diagram of 2D MPR stepper motors 29
Fig. 3.10: Motor Controller Board 30
Fig. 3.12: Photographs of the 2D MPR 32
Fig. 3.13: Photograph of 2D MPR with mounted radome 33
Fig. 3.14: Interface of the MPR (top view) 34
Fig. 3.16: Angle of rotation (Top View) 37
Fig. 3.17: FMCW pulse repetition 38
Fig. 3.18: Program Flow Chart 39
Fig. 3.19: MPR Plot Example 40
Fig. 3.20: Outline of indoor measurement site 42
Fig. 3.21: Measurement scene for experimental MPR characterization 43
Fig. 3.22: 2D image of characterized scene with small and big antenna aperture 44
Fig. 3.23: MPR with large antenna (left) and small antenna (right) 44
Fig. 3.24: Comparison of measured single target reflection as function of azimuth angle 45
Fig. 3.25: Comparison of single target reflection for different radar bandwidths 46
Fig. 3.26: 360° image in indoor environment using a bandwidth of 25GHz (left) and 5 GHz (right) 47
Fig. 3.27: Measured Reflectivity over range profile showing several reflections 48
Fig. 3.28: Comparison of results obtained by strongest scatterer and nearest scatterer approach 49
Fig. 3.29: ROS data flow (from ROS website) 51
Fig. 4.1: CAD drawing of 3D mechanical beam steering concept 55
Fig. 4.2: Circuit and Signal Flow for 3D MPR 55
Fig. 4.3: Balance points of radar (left) and antenna (right) for worst case horizontal rotation 56
Fig. 4.4: Azimuthal axis stepper motor dimensions and torque characteristics 57

Fig. 4.5: Balance points of the respective groups of the elevation rotational model 58
Fig. 4.6: Elevational stepper motor dimensions and torque characteristics 58
Fig. 4.7: 3D MPR CAD drawings 59
Fig. 4.8: Photograph of fully assembled 3D MPR 60
Fig. 4.9: Spherical Coordinate system used for MPR based image formation 61
Fig. 4.10: Front projection of 3D image generated with 80 GHz MPR with 25 GHz bandwidth 62
Fig. 4.11: Example of curvilinear MIMO array 63
Fig. 4.12: Radiation pattern of MIMO array as a function of azimuth angle 64
Fig. 4.13: 2D image with reference reflector (right) and person model (left) detected by the MPR 64
Fig. 4.14: MPR image convolved with MIMO radiation diagram for MIMO performance estimation 64

7. List of Tables

Table 3.1: Used commands and parameters of the motor controller 31
Table 3.2: Interface of the MPR 35
Table 3.3: ROS LaserScan message in MPR context 52
Table 4.1: Component groups of the azimuth rotation assembly 57

8. Appendix

8.1. **MPR Quick Start Guide**

Monostatic Pivoting Radar (MPR) - Quick Start Guide

Overview MPR

The MPR uses a FMCW-Radar for obstacle detection. It has a bandwidth of 4 GHz[1] (88 - 92 GHz), which results in a measurement accuracy of ± 3.75 cm up to a measurement range of (about) 15 m. The sweep time is fixed to 1 ms.
The MPR uses a stepper motor for rotating the FMCW-Radar. By doing this a field of view of almost 360° is covered. Only a small angle is blocked by the aluminum-profile (Figure 1). The rotation speed is determined to 2.5 Hz.

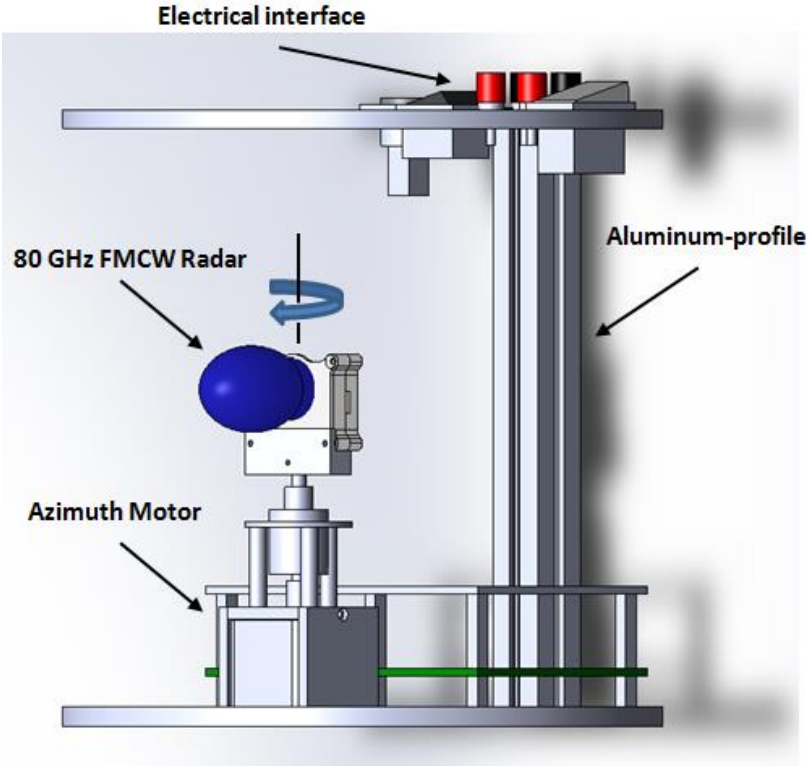

Figure 1: CAD drawing of the MPR

For a single turn 200 range measurements are made, which means one measurement every 1.8°. After this set of measurements the data is processed and the results are published by a ROS laserscan message (http://docs.ros.org/api/sensor_msgs/html/msg/LaserScan.html) with the topic **mpr_scan**. An overview about the published information can be seen in Table 1. Because of sequential data processing after collecting the measurement data, the results are published with a rate of nearly 2.4 Hz which is below the rotation speed of the radar.

The MPR provides two modes for data processing. Either the distance to the nearest obstacle can be measured or the distance to the obstacle with the

[1] The bandwidth can be increased by small changes in the MPR software, if higher measurement accuracy is needed. But in that case the measurement range will be reduced.

strongest reflection. When no target is in measurement range or it is not possible to reliably detect an obstacle, the range is set to 0 m. A data vector is formed containing the range value [m] and the intensity [dB] for each angular position. All information gained from the measurement are provided to the ROS as laserscan message (topic **mpr_scan)** containing the variables shown in Table 1.

Float32 angle_min	Start angle of the scan [rad]
Float32 angle_max	End angle of the scan [rad]
Float32 angle_increment	Angular distance between measurements [rad]
Float32 time_increment	Time between measurements [seconds]
Float32 scan_time	Time between scans [seconds]
Float32 range_min	Minimum range value [m]
Float32 range_max	Maximum range value [m]
Float32 [] ranges	Range data [m]
Float32 [] intensities	Intensity data [dB]

Table 1: LaserScan Message type overview

Interface of the MPR

All required mechanical and electrical interfaces can be found on the top of the module as shown in Figure 2.

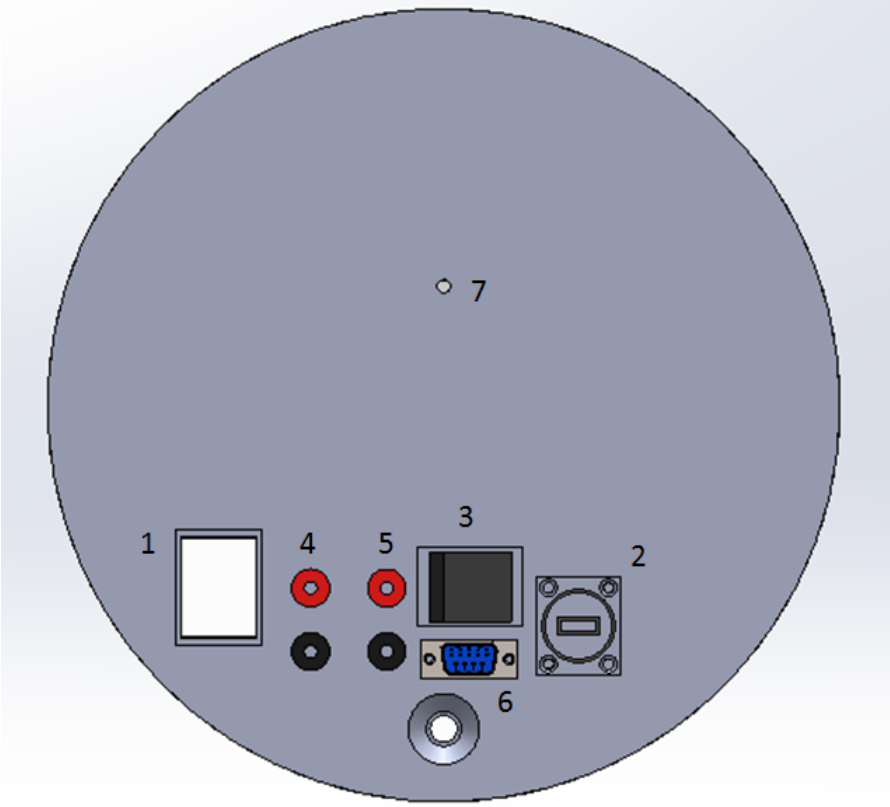

Figure 2: Interface of the MPR (topside)

The following table provides a brief description of all interfaces to ease the integration in a complete sensor suite.

Pos	Function
1	Power On/Off: This switch is used for turning the MPR on or off. Attention: If the power supply of the radar is provided by the USB interface (Radar switch (Pos 3) in position I), the radar is still active, even when MPR is turned off.
2	USB-Interface (2.0): Communication interface of the radar.
3	Radar switch: The power for the radar can be supplied either by the USB-interface (Pos 2) or by the motor controller board. For the second case the required 5V supply voltage is generated on the controller board from the controller supply voltage (Pos 4) with a fixed voltage regulator. The radar switch has the following states: Switch position I: Supply voltage for the radar provided from the USB-interface. Switch position 0: The radar is turned off. Switch position II: Supply voltage for the radar provided from the motor controller board.
4	Supply voltage for motor controller board: The supply voltage for the motor controller board can be chosen within a voltage range between 8 V (DC) and 24 V (DC). If the radar is supplied by the motor controller board, the input voltage should not exceed 12 V (default: 8V) in order to reduce the thermal leakage power. When the supply voltage for the radar is provided by the USB-interface, then 24 V can be applied. By doing this, it is possible to connect motor controller voltage (Pos 4) and motor voltage (Pos 5) in parallel. The current consumption of this voltage input is about 70 mA or about 700 mA if the radar is also supplied by the motor controller board
5	Supply voltage for stepper motor: 24 V (DC) While accelerating the motor after start, the current consumption is about 400 mA. When final speed is reached (after 5 seconds) the current consumption is reduced to approximately 70 mA.
6	Communication interface for the motor controller: Serial interface (RS232). This interface needs a 9 pole serial cable (RX and TX must not be crossed).
7	Mounting option for additional devices: The threaded hole (M5) is located at the axis of rotation of the radar.

Table 2: Interface of the MPR

Starting up the MPR

The MPR should be wired as described in the table above (Table 2).
Before using the MPR, the fftw3 library has to be installed (**sudo apt-get install fftw3-dev**).
After that two new folders have to be created in the catkin workspace and the mpr files should be copied to these folders:

- In the directory **/catkin_ws/src** create the folder **mpr** and copy the file **package.xml** to this new folder
- In the directory **/catkin_ws/devel/lib** create the folder **mpr** and copy the file **mpr** to this new folder

Further installation instructions for the MPR node can be found in the belonging README.

After starting the roscore, the MPR node can be started by the MPR executable or via **rosrun mpr mpr**. Without any arguments, the default parameter will be used.
Following arguments are available for the MPR node (e.g. rosrun mpr mpr -h):

Argument	Function
-m	define motor com port: e.g. -m /dev/ttyUSB0
-r	define radar com port: z.B. -r /dev/ttyACM0
-l	list available ttyUSB (motor) and ttyACM (radar) devices
-s	send stop command to motor: In particular cases it is possible, that the motor will not stop, although the MPR node has been closed. In this case the motor can be stopped separately by using this argument.
-n	run without motor: The radar takes measurements at the actual motor position(there will be no motor movement).
-v	activate verbose mode (for further information about internal program states and communication)
-t	set threshold level (default 3.0): The measured range spectrum is compared with a detection threshold in order to gain the distance between radar and obstacle. The threshold is set by linear decimal (not logarithmic). e.g. -t 2.5
-d	set detection mode (default 1): 0 = Distance to the nearest obstacle. 1 = Distance to the obstacle with the strongest reflection. e.g. -d 0
-h	show help

Table 3: Arguments for MPR node